TERASENSE: THz Device Technology Laboratory. Final Summary

M. Barba[6], A. García-Pino[3], E. González-Sosa [8], J. Gutiérrez[1], J. Montero-de-Paz[9], J. Parrón[7],
J. Romeu[2], P. de Paco[7], J.A. Encinar[6], L. E. García-Muñoz[9], B. González-Valdés[3][5],
E. Nova[2], R. Vera-Rodríguez[8], K. Zeljami[1], A. Badolato[4], J.L. Besada[4], T. Fernández[1],
J. Fierrez[8], J. García[6], J.M. Gil[6], M.A. González[6], J. Grajal[4], G. Junkin[7], C.A. Leal
Sevillano[6], J. Marín[7], B. Mencía[4], O. Menéndez[7], J.R. Montejo[6], J. Ortega-García[8],
J.E. Page[6], J.P. Pascual[1], G. Pérez-Palomino[6], J.M. Rebollar[6], O. Rubiños-López[3], J. Rubio[6],
J.A. Ruíz[6], D. Segovia-Vargas[9], A. Tazón[1], J. Zapata[6]

[1] Dpto. Ingeniería de Comunicaciones. Edificio Ingeniería de Telecomunicación, Profesor José Luis García García. Plaza de la Ciencia, S/N. 39005. Santander. Universidad de Cantabria (UNICAN).Spain - jessica.gutierrez@unican.es

[2] Dpt. Signal Theory and Communications. Universitat Politècnica de Catalunya (UPC)
Jordi Girona 1-3, 08034 Barcelona. Spain - romeu@tsc.upc.edu

[3] Depto. de Teoría de la Señal y Comunicaciones, Univ. de Vigo (UVIGO).
ETS Ingenieros de Telecomunicación. Campus Universitario 36310 Vigo. Spain - oscar@com.uvigo.es

[4] Departamento de Señales, Sistemas y Radiocomunicaciones, Univ. Politécnica de Madrid (UPM).
E.T.S.I. Telecomunicación. Ciudad Universitaria 28040 Madrid. Spain - jesus@gmr.ssr.upm.es

[5] Northeastern University of Boston. 360 Huntington Ave Boston, MA 02115, United States

[6] Grupo del Departamento de Electromagnetismo y Teoría de Circuitos. ETSIT. Universidad Politécnica de Madrid.
Ciudad Universitaria 28040 Madrid. Spain - mariano.barba@upm.es

[7] Departament de Telecomunicació i d'Enginyeria de Sistemes. Universitat Autònoma de Barcelona (UAB)
Edifici Q, Campus de la UAB, 08193 Bellaterra (Barcelona). Spain - josep.parron@uab.es

[8] Biometric Recognition Group - ATVS, Escuela Politécnica Superior, Universidad Autónoma de Madrid (UAM), Avda.
Francisco Tomas y Valiente, 11 - Campus de Cantoblanco - 28049 Madrid. Spain - ruben.vera@uam.es

[9] Departamento Teoría Señal y Comunicaciones, Universidad Carlos III de Madrid (UC3M), Avda. Universidad 30,
28911, Leganés. Spain - dani@tsc.uc3m.es

Abstract- **The use of THz frequencies, particularly W and G band allows reaching higher resolution and deeper penetration in emerging applications like imaging, sensing, etc.**

The development of those new applications lays on reliable technologies, background of expertise and know-how. The CDS2008-00068 TERASENSE CONSOLIDER project has given the opportunity to extent upwards in frequency the previous background of the microwaves research group partners. This article summarizes the developments of the TERASENSE work package "THz Device Technology Laboratory".

I. INTRODUCTION

This paper compiles the developments and activities of the workpackage called "THz Device Technology Laboratory" of the TERASENSE project in the frame of the CONSOLIDER program updating the results presented in [1]. The objective of this workpackage was the development of technological activities, up to THz frequencies [2],[3] covering generic technologies for active devices and passive circuits, extraction of models of new devices from DC-RF measurements, design and characterization of devices, MMICs and subsystems. All, keeping in mind that the final applications of these technologies are mainly imaging and sensing systems, which require additionally technologies for data processing [4]-[9].

The interest of the scientific community and the industry in the development of systems working in the W-band atmospheric window is increasing. In the remote sensing area millimeter waves (mmW) offer a good tradeoff between spatial resolution (using relatively small antenna apertures) and material penetration [10],[11]. Moreover, the large available bandwidth and the small system wavelength allow the development of compact wireless high speed communications systems.

The added value of emerging applications in THz bands is divided in different stages starting from the basic active devices and ending with the data processing software. Unfortunately there is a lack of basic active devices (diodes and transistors) manufactured in Spain, and very limited in Europe but there are opportunities for innovation in antenna manufacturing, in design and assembling of circuits and systems and in data processing software.

The antenna design at these frequencies represents a challenge due to the small tolerances required in the construction. Furthermore, the aforementioned mmW applications usually employ electrically large antenna apertures, requiring tens of meters between the antenna under test (AUT) and the probe antenna for the radiation pattern measurement. Therefore, performing far-field (FF) measurements to retrieve the radiation pattern is not feasible unless a compact range measurement system is used. Measuring the antenna gain with a calibrated probe in the FF represents the same problem.

About the available devices and technologies, characterization, modeling and simulation of passive and active devices becomes much more critical to succeed than in microwave circuits and demands intensive use of tools for simulation of active devices and passive structures (with 2D and 3D EM simulators). The accurate knowledge of the

properties of dielectric materials, such as those used to manufacture substrates, radomes, or lens antennas, is essential to carry out the design of devices and circuits in the mentioned frequency range. Taking into account the previous experience of the research groups, the design and characterization of circuits operating in these frequencies involved a scale reduction in dimensions, compared to previous expertise in mm-wave circuits, below the limits of previous minimum resolution for printed microstrip/coplanar circuits and mechanical tolerances in tooling. The upgrade of measurement equipment involved not only the acquisition of new apparatus, but also the change to new connectivity standards.

One of the emerging applications of the millimeter-wave imaging technology is its use in biometric recognition. This is mainly due to some properties of the millimeter-waves such as their ability to penetrate through clothing and other occlusions, their low obtrusiveness when collecting the image and the fact that they are harmless to health. This is in contrast to biometric traits acquired in the visible spectrum, which are normally affected by, among other factors, lighting conditions and occlusions (e.g., clothing, make up, hair, etc.). Section VII describes a biometric recognition system which uses body images acquired at 94 GHz.

Therefore a jump to THz frequencies meant a challenge in all the aspects: modeling, simulation designing, assembling, measurement, etc... The TERASENSE project has given the opportunity to extent upwards in frequency the huge background of the microwaves research group partners.

This article will focus on the development of technology aspects by the TeraSense partners: antenna manufacturing, characterization of active and passive devices, design and assembling of circuits and data processing.

II. ANTENNA MANUFACTURING

All referred THz applications require, as input element, an antenna, whose performance becomes critical for the system but employing a normally affordable technology. Different developments of antennas have been done in the frame of TeraSense.

A. Linear Patch Antenna Array excited by Slot

A linear array based on three patch antennas excited by slots in W band, has been designed and presented in [12]. The objective has been to obtain an antenna with high directivity, a gain about 13 dBi and a -10 dB bandwidth of 7 GHz, centered at 96 GHz. This task has been developed by UNICAN.

For this goal, initially, a single radiant patch has been designed and optimized its dimensions, obtaining suitable gain and matching, taking each patch formed by a radiant element patch (1×1.1mm) and a slot (0.7×0.09mm). It is obtained a -10 dB bandwidth of 4 GHz at 96 GHz and a directivity of 9.38 dBi with a remarkable backward radiation due to the absence of a below metallic plane.

After validating simulation results of this single patch, two more identical patches were introduced obtaining a good matching and gain, with weak back radiation. The phase center length between patches is 2.2mm and each patch is fed by 100 Ω microstrip lines (length = 3.7 mm and width = 0.09

mm) and feed lines are connected each other to a 50 Ω microstrip line (width = 0.26 mm) which, at a distance of 0.5 mm, is enclosed in a cut-off waveguide (dimensions 1.14 mm × 0.55 mm), in order to propagate only the Quasi-TEM microstrip mode in W-band, from 75 up to 110 GHz. Furthermore, the distance from the feed line to the bottom of the case is 0.5 mm.

The structure of the array has three dielectric layers with their respective metallization. The deeper layer uses the low cost Rogers ULTRALAM 2000 substrate (ε_r = 2.5, tgδ = 0.0019 and a copper thickness of 18 μm) with a dielectric thickness of 4 mils to avoid unwanted higher modes propagation. This layer contains the 100 Ω feed line located at its rear face and the ground plane where the slots are settled at the top face of the same layer. The intermediate layer is the radiant substrate, air in this case, with a thickness of 5 mils. Two side metalized supports composed of Rogers RT/Duroid 5880 substrate (h = 5mils), have been necessary to hold over the air gap the top layer, which also uses Rogers RT/Duroid 5880 with a dielectric thickness of 5 mils (εr = 2.2 and tgδ = 0.0009) and acts as a radome.
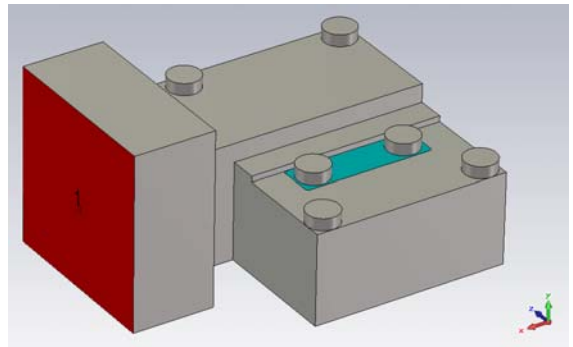

Fig.1. Patch Antenna Array with the Waveguide-to-Microstrip Transition

A PNA-X Microwave Network Analyzer with auxiliary Millimeter Wave VNA Extenders in the input and output ports, which present WR-10 waveguide inputs, is used. Therefore, a waveguide-to-microstrip transition, which matches the 50 Ω-microstrip input impedance of the antenna array structure to the WR-10 waveguide (input of the VNA Extenders), has been necessary to include it in the design to make a more realistic version of the structure (this design it is shown in subsection VI.A). Moreover, other details to become a more realistic structure, like input flange or metallic screws to put together the different layers and the pieces of the metallic structure, were included in the final design.

Finally, the complete design composed of the linear array along with the waveguide-to-microstrip transition (see Fig.1) has been evaluated showing no degradation of the array behavior.

From the results that will be shown below, it can be seen the input matching of the linear array with a -10 dB bandwidth over 7 GHz centered approximately at 96 GHz with suitable phase behavior. Moreover, it can be observed that the undesired resonances are out of the frequency band of interest. Regarding the antenna gain, a good value around of 13dBi at 96GHz is obtained according to the number of patch elements of the array. Finally, in the radiation patterns (azimuth and elevation planes) at 96GHz a backward radiation of -25dB Main Lobe Level and a -14dBi Side Lobe Level, typical value in this type of structure, can be seen.
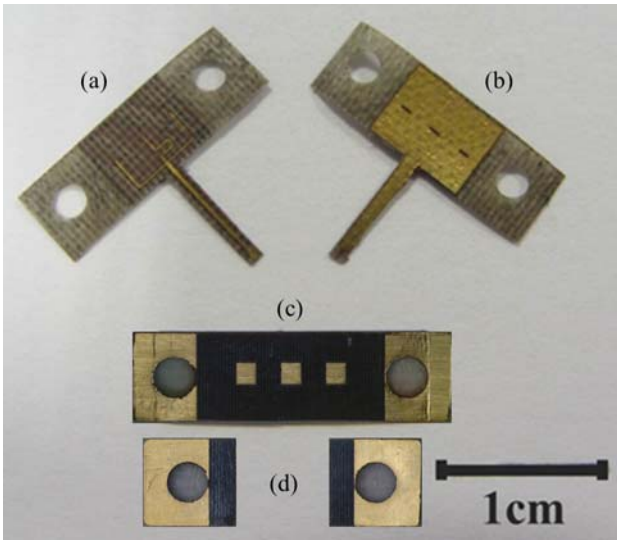
Fig.2. Photographs of the Microstrip Lines for the Complete Radiant System. (a) Feed Lines and Microstrip Lines of the Waveguide-to-Microwave Transitions, (b) Slots, (c) Three Array Patches and (d) Two Side Supports

After approving the simulation results the antenna prototype was made up in two stages: the radiant elements and the metal case [13]. On the one hand, the feed lines have been designed following the procedure introduced in section II. In Fig.2, the layers that constitute the complete radiant system can be seen.

Fig.3. Photograph of the open Metal Case for the Patch Antenna Array

On the other hand, the entire metal case has been split in two pieces (see Fig.3). The suitable cutting plane has been located in order to contain the entire cutoff cavity in one half avoiding undesired resonances due to possible defects. The final dimensions of the metal case are $4 \times 3 \times 1.5$ (all in cm).
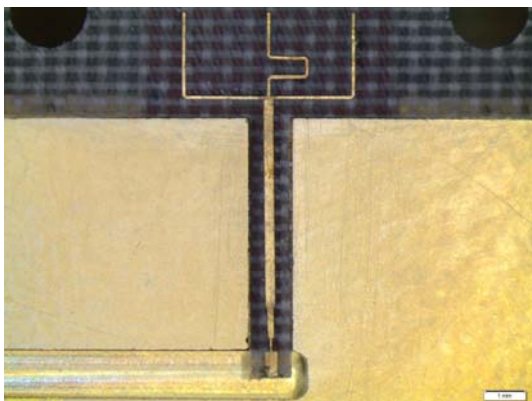

Fig.4. Zoom of the Deeper Layer within the Complete Radiant System

Finally, all layers are placed within the metal case to complete the assembling of the prototype. A detail of the upper layer soldered on the metal case is displayed in Fig.4 and the complete prototype can be seen in Fig.5.

Fig.5. Final Prototype of the Antenna

Regarding to the experimental measurements, input matching, gain and 2D radiation patterns have been done using a N5242A PNA-X Microwave Network Analyzer, with two auxiliary Millimeter-Wave VNA extension modules to expand the analyzer to millimeter frequencies, specifically to W-band (both heads present WR-10 waveguide access) [14].

All measurements have been done in far field conditions. The prototype antenna was placing at the port 1 head to measure the input matching and afterwards, the gain was obtained from two steps. In first place, two identical horn antennas previously characterized were placed in the setup, measuring their S_{21} value. Then, one of these horn antennas was replaced by the antenna array under test, obtaining its realized gain, adding the differential value between the actual S_{21} and the previous S_{21} parameter, to the horn antenna gain.
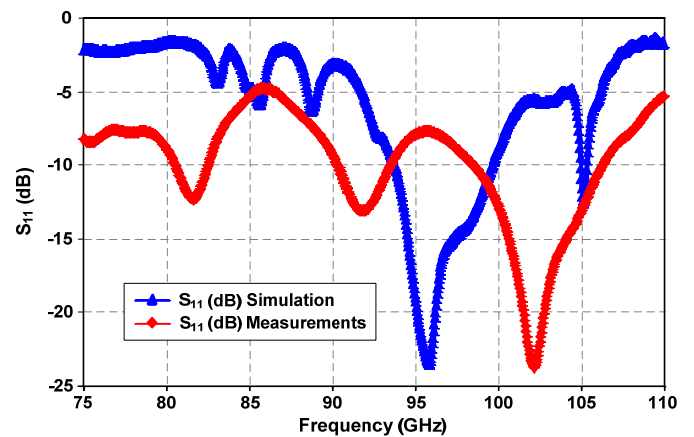

Fig.6. Comparison of the Input Matching between Simulations and Measurements

A comparison between simulation and measurement results of the input matching it is shown in Fig.6. From these results, we can see a good response with similar values although a frequency shift is observed, being the minimum S_{11} simulated at 96GHz and the minimum S_{11} measured at 102.2GHz. This deviation could be due to the tolerance in the air gap between the slots and the patches.
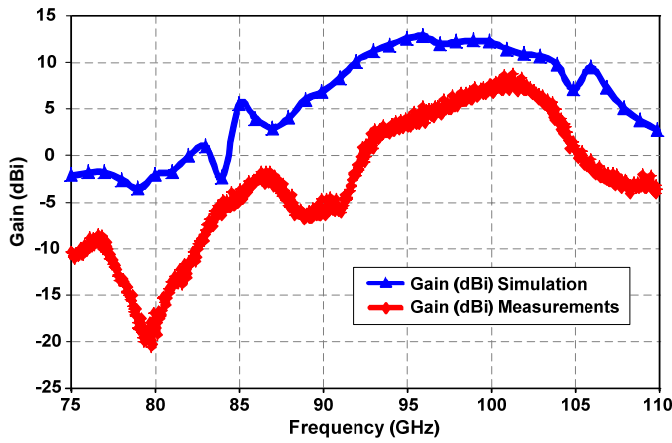
Fig.7. Comparison of the Gain between Simulations and Measurements

The gain obtained in the laboratory was compared with the simulation results too. In this way, we can observe (see Fig.7) that the shape of both results is quite similar in the range of frequency. This difference (about 4dB) can be due to additional losses of the transition, accesses, setup used, etc…
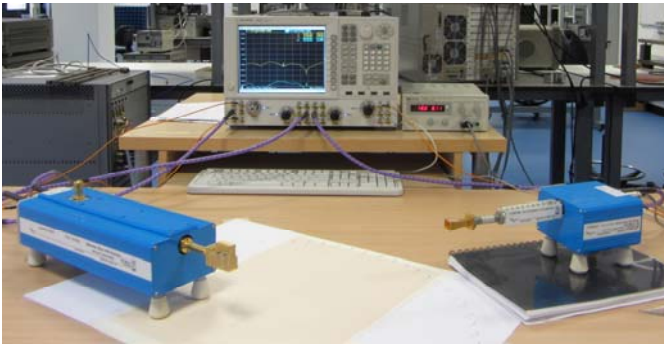

Fig.8. Setup for the 2D Radiation Pattern in Azimuth Plane

Regarding to the radiation features, the radiation pattern in far field was obtained from two measurements. The setup of the laboratory for the elevation plane is shown in Fig.8, where the antenna array was placed in the port 1 and the horn antenna in the port 2. The scanning was made from -65˚ up to +65˚ in a 5 degrees step, moving the horn antenna respect to the array.
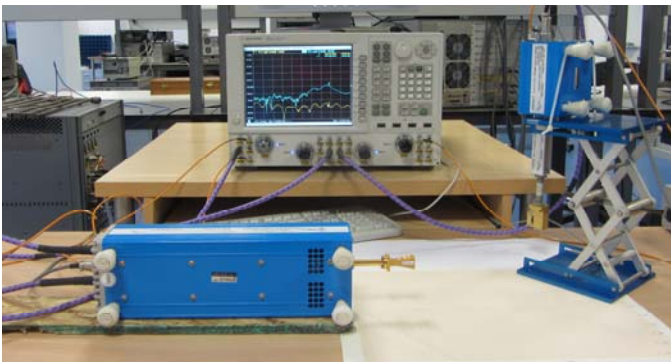

Fig.9. Setup for the 2D Radiation Pattern in Elevation Plane

To obtain the elevation plane in a simple and easy way (see Fig.9), the horn antenna was placed in this case in the port 1 and the antenna array in the port 2, turning its position in vertical sense respect to the measurements plane. Movement for obtaining the azimuth plane was done by the

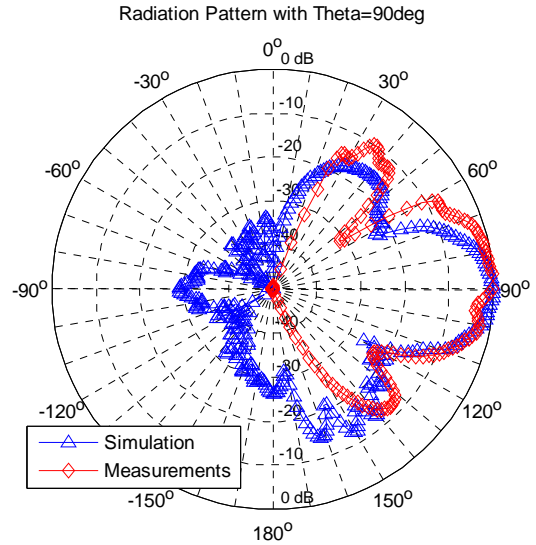horn antenna, scanning from -65˚ up to +65˚ in a 5 degrees step.

Fig.10. Radiation Pattern of the Azimuth Plane: Simulations and Measurements Results

Measured input matching of the antenna array in far field conditions is compared with simulated results in Fig.10 and Fig.11 (Radiation patterns represented at the minimum return loss frequency: 96GHz for the simulations and 102.2GHz for the measurements). We can observe an excellent result of the antenna array prototype with respect to the desired behavior. We can highlight the good value and shape of the side lobules regarding the main lobule in the elevation plane, as well as a lack of directivity in the other plane as it was expected.
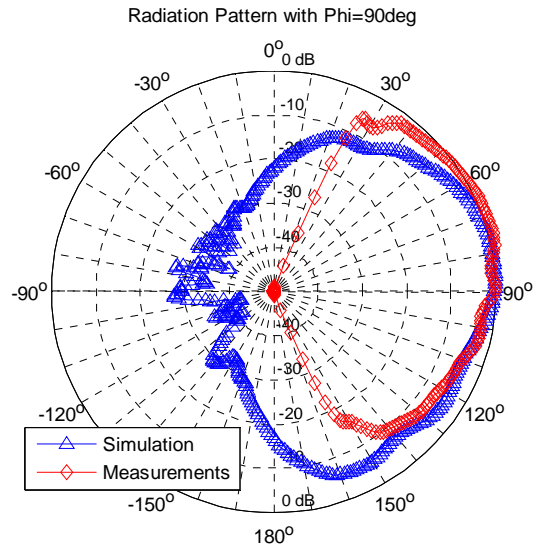

Fig.11. Radiation Pattern of the Elevation Plane: Simulations and Measurements Results

For the enhancement of the directivity in the elevation plane the addition of a chiral metamaterial cover composed by 7×5 aligned pairs of rosettes is proposed [15],[14]. Each unit cell consists of two planar metallic rosettes (radius = 166µm, width = 80µm) printed on both sides of a substrate (h = 6mils and copper thickness = 18µm), placed in parallel and one of them is twisted a certain angle (15˚ in this case) respect to the other one. This condition provides the property of 3D chirality to this structure.
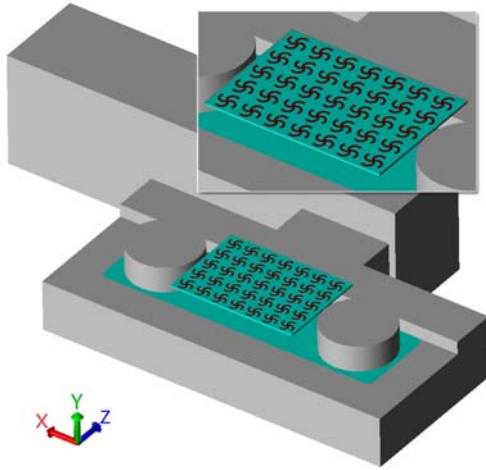
Fig.12. Antenna with Chiral Metamaterial Cover. Inset: Zoom of the Cover

This cover is placed above the antenna array at a certain distance of it and between the two lateral screws, parallel and aligned to the radome (Fig.12).
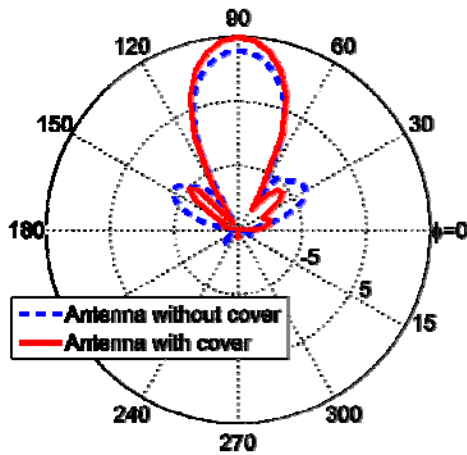

Fig.13. Radiation Pattern with and without Cover in the Azimuth Plane

A comparison of radiation pattern (azimuth in Fig.13 and elevation plane in Fig.14) simulation results with and without the cover. An enhancement of 2dB (from 13dBi to 15dBi) is obtained with the cover and the Side Lobe Level decreases 4dB (from -16dB up to -20dB). Moreover, on one hand, in the elevation plane, the chiral metamaterial focuses the radiation pattern in the broadside direction, reducing the 3dB beamwidth 21˚ (decreasing it from 57˚ to 36˚) and on the other hand, in the azimuth plane, the main lobe and beamwidth has not changed but the secondary lobes gain and beamwidth have been reduced. A deviation of 5˚ is happened in the elevation plane from the broad side direction (θ=90˚, φ=90˚) and it could be due to a slight misalignment between the three patches array and the cover.
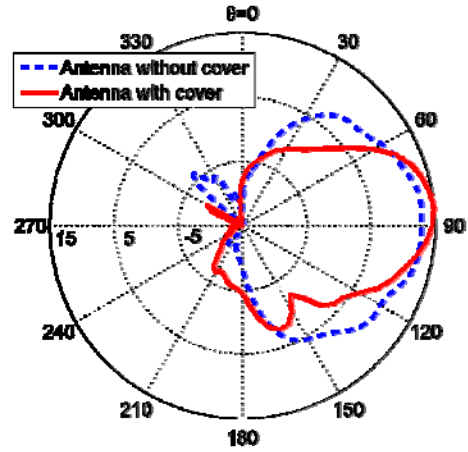

Fig.14. Radiation Pattern with and without Cover in the Elevation Plane

B. 94 GHz Cassegrain Reflector Antenna

This section presents a solution to overcome the limitations mentioned above in the design and measurement of electrically large antennas at mmW [16]. This task has been developed by UPC. The radiation pattern results obtained with a NF to FF transformation technique are shown in section B.1. Moreover, the efficiency has been measured using a radiometric technique to obtain the gain pattern. Finally, the tolerance effects in the RL for several antenna prototypes are exposed in section B.2 and a waveguide matching network is proposed to match the antenna impedance at 94 GHz.

The measurements results correspond to a 94 GHz cassegrain antenna with a main reflector of 160 mm diameter. Fig.15 shows a photograph of the antenna describing its most relevant parts. The feeder consists on a horn antenna with a Teflon top in order to have a watertight structure.
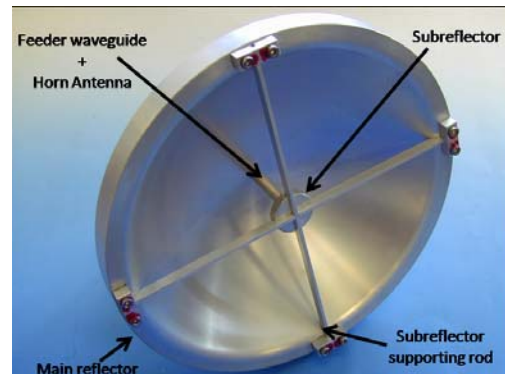

Fig.15. Photograph of the Antenna under Test

B.1. Radiation Pattern Measurement

The radiation pattern of the antenna has been obtained by transforming the measured electric field of the antenna aperture. The electrical field has been sampled each 0.45λ, obtaining a matrix of 140x140 electric field values corresponding to an area of 201x201 mm at 5 cm from the reflector aperture.

Fig.16 shows a photograph of the 2D NF measurement setup. It is composed by a W-band network analyzer with a transmitter header connected to the AUT and fixed to an

optical table. The probe is connected to the receiver and held on a 2D scanner with 300x300 mm travel. An RF absorber has been used to avoid reflections from the scanner and the receiver header.

The radiation pattern has been measured after the antenna construction, after a thermal shock test and after vibration test. Fig.17 shows the results of the E-plane, H-plane and a 45º cut of the radiation pattern measured before and after the environmental tests. It should be pointed out that the variation of the results after the environmental tests are negligible.
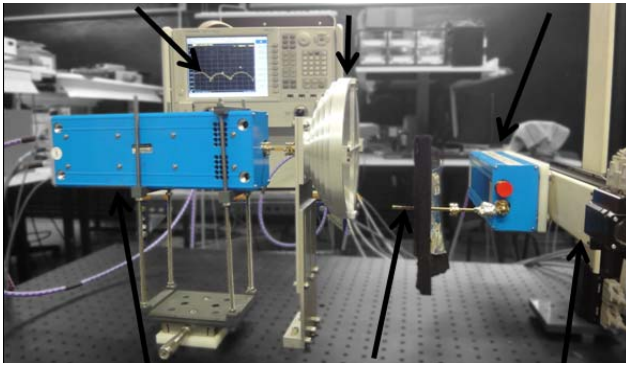

Fig.16. W-band near Field Scanning Setup

Several radiation parameters are extracted from the radiation patterns: a directivity of 41.3 dB, a -3dB beam width $\Delta\theta_{-3dB}$ of 1.42º, an E-plane side lobe level of 21.7 dB and a H-plane side lobe level of 22.9 dB.
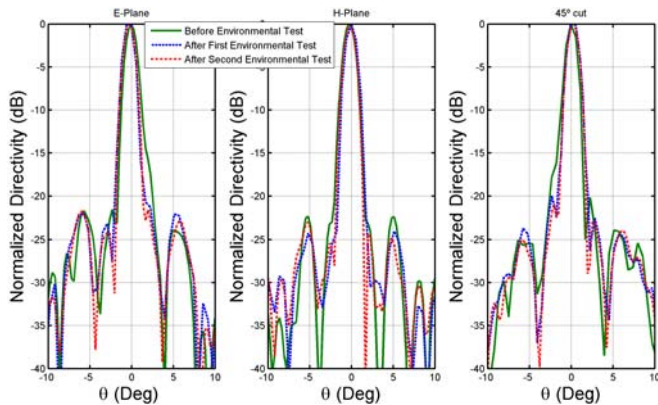

Fig.17. Measured Radiation Patterns of the Cassegrain Antenna after Construction and after Two Environmental Tests

B.2. Antenna efficiency measurement

The antenna efficiency has been measured using a radiometric technique. Fig.18 shows the total power radiometer components. The local oscillator frequency is at 94 GHz and the baseband signal is filtered at 400 MHz. Therefore the antenna losses are averaged from 93.6 to 94.4 GHz. A horn antenna has been used as a reference antenna (supposing no losses) in order to calibrate the radiometer looking to the sky using a calibrated attenuator. As a result 2.9 dB of losses have been obtained in the antenna, giving an antenna gain of 38.3 dB.
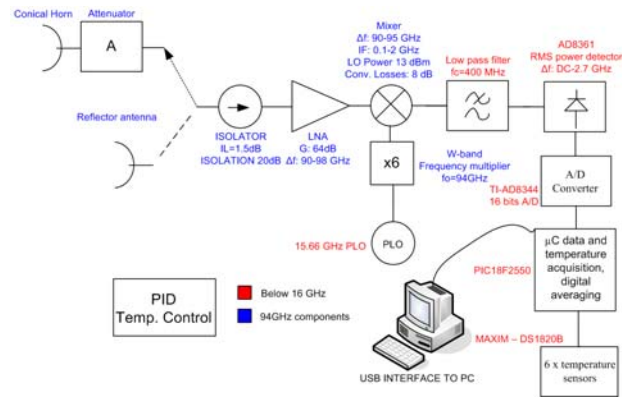

Fig.18. Radiometer Hardware Components Schematic

Due to the tolerances in the Teflon cap construction, the RL of the antenna is not matched at 94 GHz. Fig.19 shows the variability of the RL for different antenna prototypes. Using a waveguide matching network composed by 3 capacitive screws, all the antennas are matched at 94 GHz with a RL below -18 dB as shown in Fig.20.
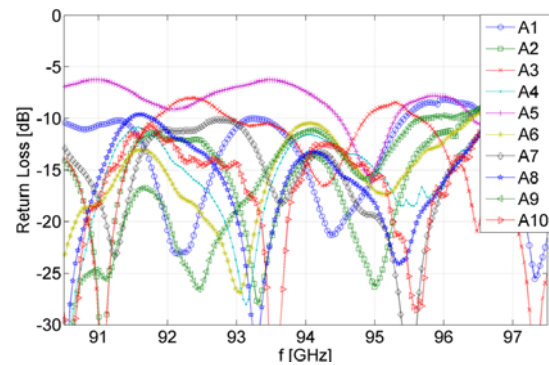

Fig.19. Return Loss of 10 Different Antenna Prototypes before Impedance Matching
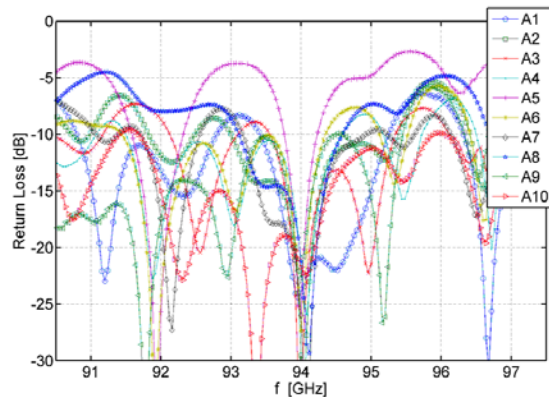
Fig.20. Return Loss of 10 Different Antenna Prototypes after Impedance Matching

C. Bifocal Reflector Antenna Prototype for Radar Imaging at 300 GHz

A 300GHz high-resolution imaging system for security applications (such as detection of weapons or concealed contraband on persons) has been developed by GMR-UPM and Antenna-UVigo groups. The system utilizes the CW-LFM (Continuous-Wave Linear-Frequency Modulation) radar technique. Its operational bandwidth goes from 286.2 to 313.2 GHz, within a window of atmospheric attenuation.

In such frequencies, a wide range of materials (clothing, paper, plastic, wood ...) is reasonably transmissive.

The radiating system utilizes Bifocal Ellipsoidal Gregorian Reflector geometry with a small mechanical rotating mirror to achieve an image resolution less than 2 cm at a standoff range of 8 m within a scanned area of 0.8 m x 0.5 m. The antenna prototype can be seen in Fig.21. It is composed of the following elements:

(a-b) The main reflector and the subreflector are shaped surfaces configured as the Bifocal Ellipsoidal Gregorian Reflector System (BEGRS) described in [17], in order to improve the scanning behavior of the antenna, provide higher field of view, increase the antenna gain in the target region and allow better control of the scanning operation. In addition, the subreflector must be oversized in order to span the field of view to the size of the human torso.

(c) In order to provide scanning characteristics, the illuminating wave arrives at the subreflector after being reflected in the mirror. The mirror is flat and lightweight. It has two rotation axes providing two different motions: a fast rotating motion about a primary axis which can be rotated slowly about a secondary axis along (vertical tilting).

(d) A feed reflector designed to illuminate the subreflector with a tapered collimated beam.

(e) A silicon beam splitter to separate the transmitted and received beams.

(f) A transmitting horn whose beam passes through the feed splitter.

(g) A receiving horn taking the reflected beam at the beam splitter.

Fig.21. 300GHz Antenna Prototype

D. Active Antennas in the W-Band based on Schottky Diodes

This section shows the development of a Schottky Barrier Diode (SBD) based compact receiver module operating in the E-band (71-76 GHz) [18].This task has been developed by UC3M. In order to achieve a compact receiver, direct envelope detection is used, avoiding the need of a local oscillator (LO) signal. The module is shown in Fig.22 and it comprises a hyper-hemispherical Si lens, a zero-bias SBD

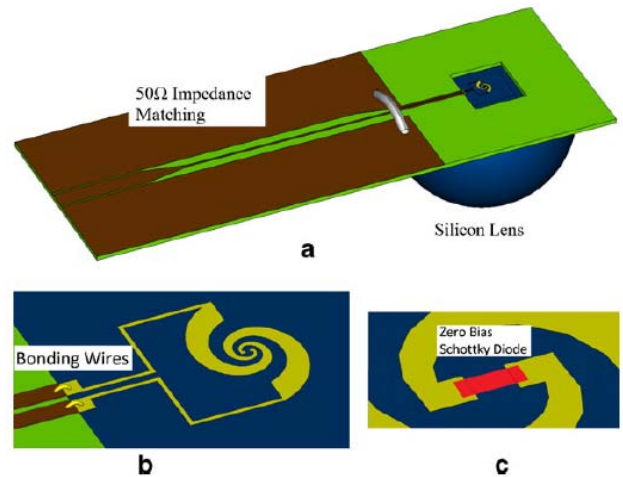which is mounted on a planar antenna, and a 50Ω low frequency impedance matching output.

Fig.22. Schematic of the SBD QO Video Detector with Log-Spiral Antenna. Materials: Dark Blue Part is the Silicon Lens and Silicon Substrate where the Gold (Yellow Part) Planar Antenna is grown, while Green Part is FR-4 Material and Brown Part is Copper. Bonding wires are included to connect gold lines over silicon to copper lines over FR-4 and a metallic wire is inserted to interconnect both ground planes of CPW line. Zero Bias Schottky diode is epoxied in the middle of the antenna. (a) Complete SBD QO Video Detector 3D schematic. (b) Antenna zoom. (c) Schottky diode zoom [18]

D.1. Receiver Design

In the design of the antenna, both gain (directivity * radiation efficiency) as well as matching between antenna and active element (antenna impedance) need to be taken into account [19]. We have designed and fabricated three different planar antenna types: Meander Dipole, Log-Spiral and Log-Periodic, to evaluate which one provides the best performance to the receiver module. Meander dipole has been designed to maximize the power delivered from the antenna to the SBD at the millimetre-wave carrier frequency range, matching the impedance of the antenna to the impedance of the SBD [20]. With Log-Spiral and Log-Periodic antennas a constant broadband response is expected.

D.2. Measurements

Three receivers were manufactured and measured within the E-Band. A picture of the Log-Spiral receiver can be seen on Fig.23.
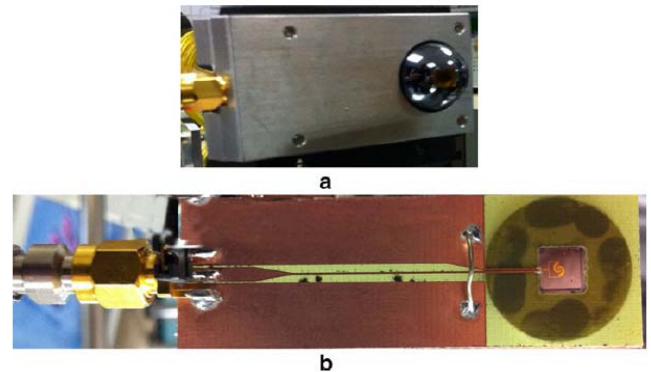

Fig.23. Photograph of the Receiver Module: (a) Front View of the Cased Module showing the Si Lens, and (b) Back View of Uncased Module, showing the Log-Spiral Antenna on HR-Si and the Impedance Matching Transition to the SMA Output Connector [18]

The measured responsivity, as the signal produced by the power arriving to the SBD receiver, is shown on Fig.24. The effective area normalized peak responsivity of the receiver in the 70-76 GHz band is found to be 814.4 V/W and 740.3 V/W for the Meander Dipole and the Log-Spiral antenna respectively. The module with log-periodic antenna exhibits a responsivity value reaching 1278 V/W at 72GHz.
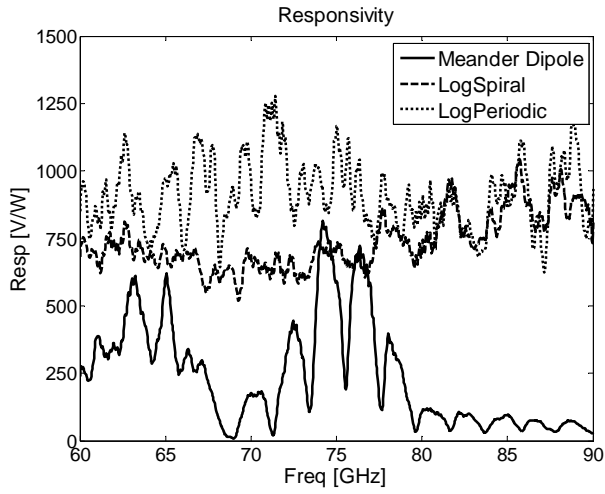

Fig.24. Responsivity Spectra Measured over the E-band for the Meander Dipole, Log-Spiral and Log-Periodic Antennas [18]

D.3. Extension to Photomixer THz Emitters

The same approach has been followed to manufacture an antenna emitter (AE) working at 1.05 THz [19]. This AE is based on a photomixer, the meander dipole antenna and a hyperhemispherical silicon lens. A schematic of it can be seen on Fig. 25 (a) and the manufactured meander dipole antenna with the photomixer is shown in Fig. 25 (b). In the traditional approach for CW THz generation by photomixing a THz current is generated in a semiconductor device using two heterodyned laser beams of photon energies $h(f_0 \pm f_{THz}/2)$ (with the same power, $P_L/2$, and polarization), differing in photon frequency by the THz frequency f_{THz} (being h the Planck constant and f_0 the central frequency). As a first step, the heterodyned laser signal is absorbed on typical length scales shorter than 1 µm, i.e. much shorter than the THz wavelength. In the second step the resulting photocurrent is fed into an antenna, which then emits THz radiation [21]. The obtained results can be seen on Fig. 26. At 1.05 THz there is an increase of 6 dB of the THz emitted power when compared with a conventional log-periodic based AE with same photomixer device.
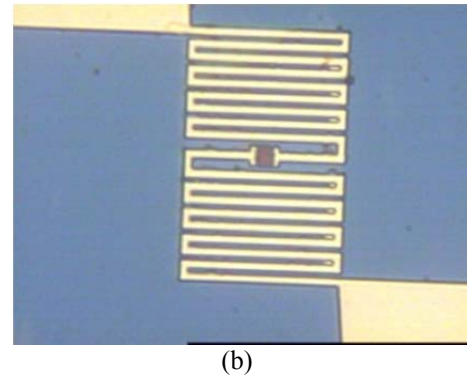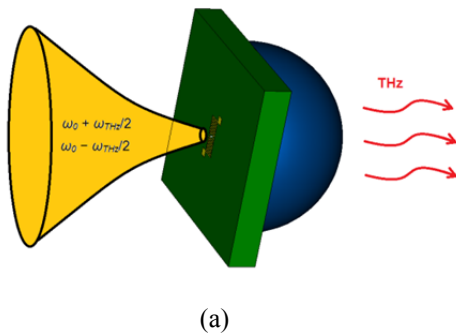

(a)

(b)

Fig. 25. (a) Schematic of an AE for CW THz Power. (b) Manufactured Meander Dipole Antenna with Photomixer Device
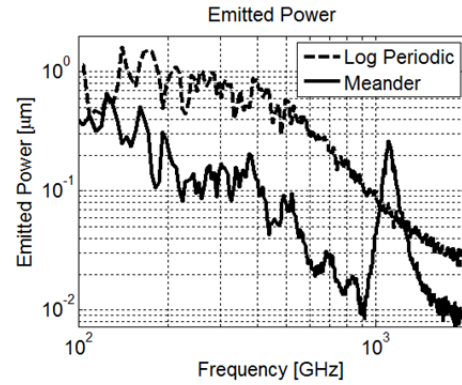

Fig. 26. Measurements of both Log-Periodic and Meander Dipole AE. A 6 dB CW THz Emitted Power Improvement is obtained at 1.05 THz

E. LC Reflectarray and Supporting Technologies

E.1. W-band Liquid Crystal Reflectarray (with Beam Scanning)

Many tasks and achievements have been finalized and reached during the last year in the LC reflectarray with beam scanning (in one plane). This task has been developed by DETC-UPM.

Some of the most remarkable are the following: a final prototype (an array with 54 rows and 52 columns) has been manufactured using the design conclusions obtained during the previous work; the electronic control system (including relay boards, USB-boxes and controls software) manufacturing has been finalized and tested; a procedure for measuring LC switching times was implemented and the times for the designed LC measured. It has to be noted that this "low frequency" characterization is essential to achieve a reliable control system for 3-D scanning. A W-band measurement system for LC reflectarray characterization was based on measurements in a quasi-optical bench was defined and implemented, which necessary to validate the accurate analysis of the electromagnetic behavior of the LC reflecting element in function of the biasing signal –amplitude, shape. Also, the angle of incidence of the RF signal has a relevant role, so the measurement system considered several angles of incidence and reflection [30º; 37.5º and 45º]. This is needed for the correct implementation of the pattern synthesis. In the same system the scanning capabilities in one plane of the reflectarray were demonstrated. This work is described in [22] and the conclusions after the experiment are included in [23].

An antenna system based on a Dual Reflector at W-Band (94 GHz – 106 GHz) using the previous LC reflectarray as subreflector, has been mounted and measured, giving the expected results [24],[25], having a beam scanning from -8º to +6º in the elevation plane, with gain greater than 30 dBi in a 10% bandwidth.

During the present year and by the end of the project a LC reflectarray with beam scanning in both planes [3-D scanning] is expected to be finalized and measured.
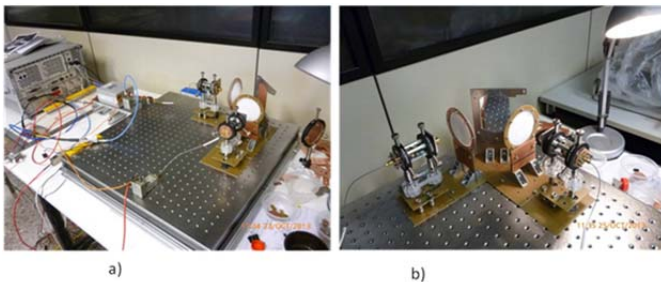

Fig. 27. LC Switching Time Measurement Setup

Fig. 28. Quasi Optical Bench W-Band LC Measurement. A) RF Calibration, (Millmimeter Wave Instrumentation: PNA-C, TR module, Mixers, and IF Amplifiers supplied by SSR (UPM)). B) Q-O Bench Calibration, 45º/45º Configuration, with mirror; c) LC RA Measurement in 45º/45º Configuration
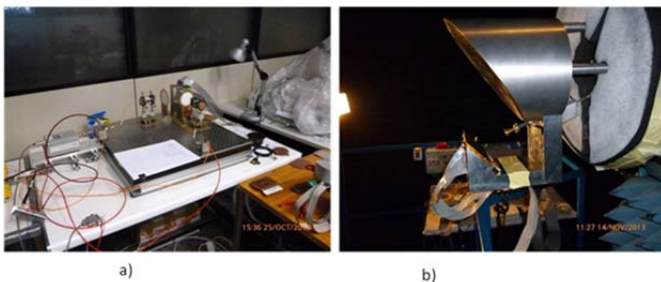

Fig. 29. a) LC RA Measurement in Quasi-Optical Bench 45º/45º Configuration, with mirror; c) W-Band Dual Reflector using the LC RA as Subreflector. (Scanning in Elevation)

E.2. Improvement and New Advanced Analysis Tools for Microwave and MM-Wave Devices

This task has been followed in two lines: one devoted to the analysis of radiation patterns and other to the efficient design of filters.

The use of spherical modes in computational electromagnetics applied to antenna problems has been reviewed. First, the theory of spherical modes is reviewed. Second, the use jointly with the Finite Element Method is exposed. Third, the application to the analysis of finite arrays is shown. Finally, we present how the spherical modes allow us to obtain an equivalent model of the antenna, in terms of infinitesimal dipoles, which increases the capabilities of the method for the analysis of finite arrays.

Methods based on Spherical Wave Expansion have proved to be greatly useful in computational electromagnetics because they provide an exact boundary condition, and they mix very well with the FEM/Modal Analysis, allowing us fast frequency and angle-of-incidence sweep, based on purely sparse matrices. Additionally, they are best suited for the analysis of the mutual coupling in arrays of arbitrary elements on a ground plane.
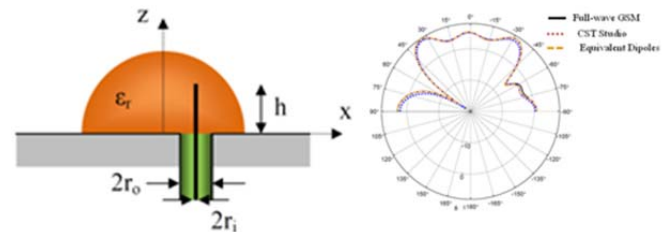

Fig. 30. Active Element Pattern of a 7x7 Array of Dielectric Resonator Antenna

A work about the Fast and Reliable Monostatic RCS Computation as a Function of Frequency and Angle of Observation via the Reduced-Basis Method has been performed. The work has been focused on a rapid and reliable frequency-parameter and angular-response sweep in monostatic RCS prediction via the reduced-basis method. This is done by understanding how these two parameters contribute to the actual physics in the problem. Spherical mode expansion is taken into account to truncate the computational domain. Special attention is given to come up with a formulation dropping singularities in the frequency axis out of the Maxwell operator. As a result, we directly work with an S-formulation for the Maxwell system. A model order reduction approach where field solutions at different parameter values are used as new basis for Galerkin projection has been proposed. In addition, the accuracy of the reduced-order model is certified by means of the residual error of the reduced field solution throughout the whole parameter band of interest. As a result, a fully automatic and completely reliable model order reduction process is achieved. Several radar signature images both for frequency and observation angle in real-life applications have been computed to illustrate the capabilities of this approach.

A work for Fast and Accurate Design Tools for Microwave Filters via Domain Decomposition Methods in FEM and Reduced-Order Models has been also performed. When developing a design by means of an optimization technique, the analysis domain is typically modified, e.g., its shape, the electromagnetic properties of the materials or their shapes, until the required specifications are satisfied. It seems that the global structure ought to be analyzed each time a modification is carried out. What it is proposed is to isolate the small portion of the domain that has been changed and thus concentrate on the analysis of those parts that evolve. In order to carry out this strategy, a direct domain decomposition approach in the FEM is considered, and thus, the subdomains are electromagnetically described by fullwave matrix-valued transfer functions, namely, generalized scattering matrices.

Once these transfer functions are determined, the response of the overall system is recovered by the scattering matrix connection. This methodology is compatible with a

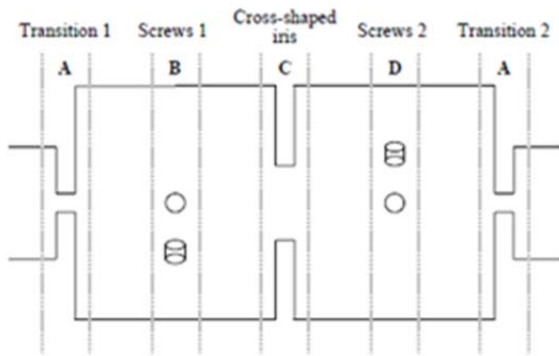reduced-order model approach and, as a result, a reliable fast frequency sweep technique is carried out.

Fig. 31. Side View of a Four-Order Dual-Mode Circular Waveguide Filter

E.3. Supporting Technologies for Beam Forming Networks

The development of silicon micromachined band pass filters in the WR-1.5 band (500 to 750 GHz) has been recently presented [26]. The deep reactive ion etching (DRIE) silicon micromachining process developed by NASA Jet Propulsion Laboratory, USA was used for the fabrication of these filters. Two canonical topologies based on E- and H-plane were implemented. Experimental results have shown better than 10 dB return loss and approximately 1 and 2.5 dB insertion loss (for 6% fractional bandwidth) for the E- and H-plane topology, respectively. The obtained results are in agreement with micron fabrication tolerances and trench angles up to 3°.

Different waveguide duplexers have been developed at 100 and 225 GHz [27] with successful results. This is a new duplexer concept design appropriate for microwaves and submillimeter wave bands with several advantages against current duplexing alternatives. The main advantages are compactness, low loss, single antenna, ferrite and magnet-free and lack of quasi-optical elements. The designed duplexer is a fully waveguide component that can be easily integrated in a radar system. Measured results show a return loss better than 20 dB, isolation of 30 dB and axial ratio below 1 dB in a more than 10% fractional bandwidth. The prototype at 225 GHz has been developed at the NASA Jet Propulsion Laboratory, USA and has been already integrated in a radar front-end. The 100 GHz prototype is being set in the Terasense image radar and system performance results will be obtained soon.
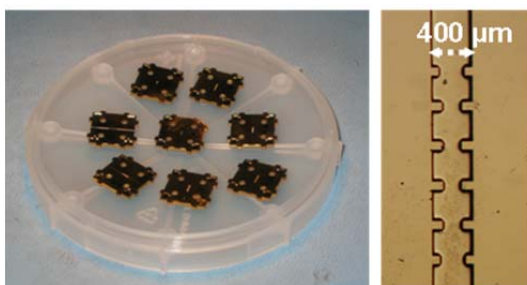

Fig. 32. Micromachined Band Pass Filters at 500-750 GHz

Fig. 33. Circular Polarization Waveguide Duplexer (Horn + Septum-OMT) at 100 and 225 GHz

A new high-performance wideband waveguide band-pass filter operating in W-band (75-110 GHz) has been modeled, manufactured and measured [28]. This filter has several potential applications and will particularly be relevant in radio-astronomy receivers. Two different prototypes were fabricated using an accurate electroforming machining technique. It is noteworthy the low level of insertion losses (around 0.4 dB within the band-pass) compared with previously developed filters [29]. This work was carried out in collaboration with Jodrell Bank Center for Astrophysics, School of Physics and Astronomy, The University of Manchester, Manchester, UK.

The design of an orthomode transducer (OMT) for dual-band operation and optimized for stacked micro-machined layers implementation has been accomplished [30]. The proposed design avoids the use of critical elements and minimizes the number of equal-thickness micro-machined layers required. In this way, the micromachining fabrication is simplified, making the proposed design a very attractive candidate for high frequency applications and for low-cost batch production. A W-band dual-band design with more than 10% fractional bandwidth for each band and 30% separation between bands was designed. Two OMTs in a back-to-back configuration have been fabricated using a thick SU-8 photo-resist micromachining process. The experimental results validate the proposed OMT geometry and its micromachining implementation. This work was carried out in collaboration with the University of Birmingham.
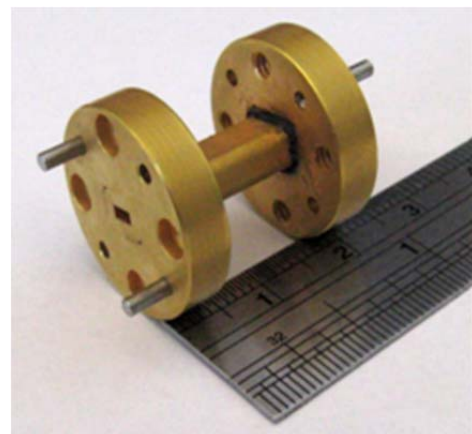

Fig. 34. Tenth Order W-band Band Pass Filter for Radio-Astronomy Receivers

Fig. 35. Dual-band SU-8 Micromachined OMTs

III. CHARACTERIZATION AND MODELING OF BASIC ACTIVE DEVICES

As it was previously mentioned, the fabrication of basic active devices (transistors and diodes) to operate in THz bands is nowadays completely out of the scope of the project. It is not possible at all to compete with companies (mainly in USA) with a background of decades and a strong government support in space and military programs.

Luckily, some devices are commercially available, like high performance diodes from Virginia Diodes. Such Diodes may be essential part of detectors, mixers and multipliers.

Those subsystems may be designed and assembled in affordable hybrid technology, but requiring accurate modeling to achieve success.

Schottky diodes are used for design of detectors, mixers and frequency multipliers in sub-millimeter wavelengths. In addition, the planar diode opens up the possibility of diode circuit integration.

In this section an ultra-wideband (DC to 110 GHz) model, for a single Anode Schottky Diode (Virginia Diodes VDI) is presented [31],[32]. This task has been developed by UNICAN. Model extraction is based on different measurements [33] and computer-aided parameter extraction have been performed to obtain a complete large-signal equivalent circuit model suitable for the device under consideration up to 110 GHz, and for its integration in planar circuits. Measurements were: direct current (DC) characteristics, capacitance measurements, scattering (S) parameter measurements and measurements of the assembly of Coplanar to Microstrip bonded transitions used to achieve the complete final diode model up to 110 GHz [34]. In accordance with the availability of measurement equipment, the measurements were carried out in two frequency ranges: DC-50 GHz and 75-110GHz. To verify theoretical models of the Schottky diode, biased measurements are done to measure the characteristics of the junction capacitance.

A. Direct current (DC) Characterization of Schottky Diodes

A Schottky Diode can be modeled as a combination of resistance and capacitance, both bias-dependent. The Schottky diode model consists of both, linear and nonlinear parts. The nonlinear part corresponds to the metal-semiconductor junction, and the linear part contains everything else. An accurate modeling of parasitic effects introduced by the diode package elements is necessary. Several studies on diode modeling have been done.

A widely recognized model is the thermionic-field emission model generalized I-V characteristics, equation (1),

capacitance-voltage relationship, taking into account the dependent junction capacitance, has been given by (equation 2):

$$I(V_d) = I_s\left[\exp\left(\frac{q(V_d - I_d R_s)}{\eta k T}\right) - 1\right] \approx I_s \exp\left(\frac{q(V_d - I_d R_s)}{\eta k T}\right) \quad (1)$$

$$C_j(V) = \frac{dQ}{dV} = \frac{C_{j0}}{\left(1 - \frac{V_j}{\phi_{bi}}\right)^\gamma} \quad (2)$$

Fig.36 shows the measured DC I-V, and C-V data, compared with the model (comparison between on-wafer S-parameter measurements and with low-frequency measurements using a LCR meter [35]. As can be seen, the model predicts quite well all these measurements.
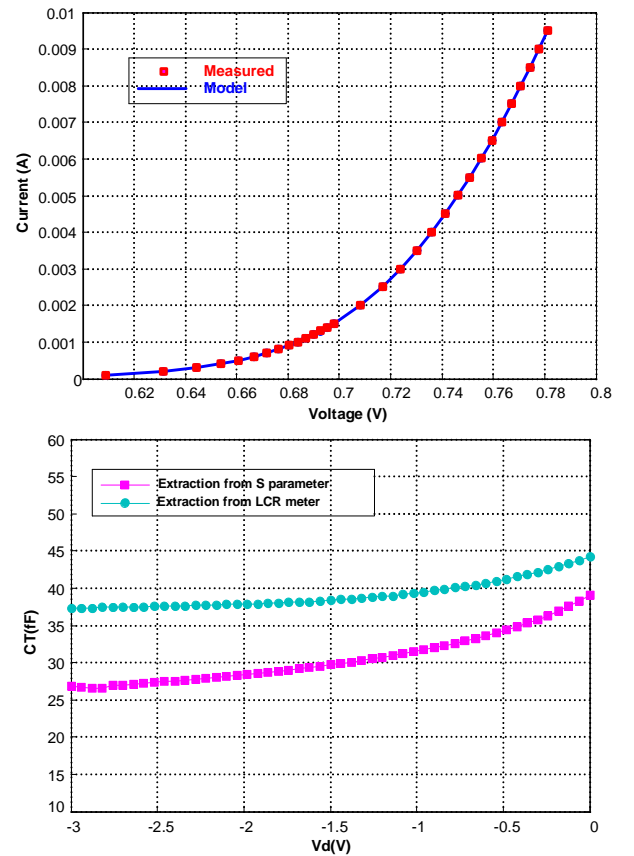

Fig.36. DC I-V Curve, and C-V Measurements and Simulations

B. Characterization of Diode: Simulation (Modeling Tools)

Voltage dependency of $C_j(V)$ and $R_j(V)$ can be implemented using a SDD (Symbolically-Defined-Device) module from ADS. Fig.37 shows a Single Anode Diode (SA-Diode) under consideration. The nominal overall chip dimensions of the diode are 600μm × 250μm × 100μm (length x width x thickness). It is connected with coplanar-to-Microstrip transitions (model PROBE POINT TM0503 JmicroTM transition). This configuration allows enabling on-wafer measurements using air coplanar probes, but in this case requires the use of wire bonding connections.
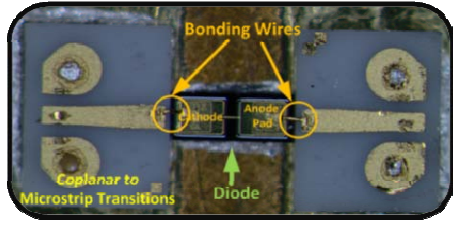
Fig.37. Single Anode Diode bonded with Gold Wires (Diameter of 17µm and Length 200µm-210µm at both Sides)

C. Equivalent Circuit Model of the Diode (Lumped Elements: Intrinsic and Extrinsic)

Fig.38 shows the equivalent circuit proposed for the discrete planar Schottky diode under consideration in order to illustrate its integration in a microstrip circuit environment including bonding wires. The circuit includes a finger inductor L_p (estimated using the planar inductor approximation) and a pad-to-pad capacitor C_{pp}. In parallel with the Schottky junction is the finger-to-pad capacitance component C_p. A set of simple lumped elements models parts inside and outside the diode: an ideal inductance L_2 in series with resistor R represents the wire inductance and losses due to the metallization and wire bonding, as well as radiation losses at the wire bends. The two shunt capacitances close to the input and output ports (C_1, C_2) represent the substrate capacitance between the microstrip lines onto which the wire is bonded. The inductor L_1 represents end inductance caused by the wire bonds.
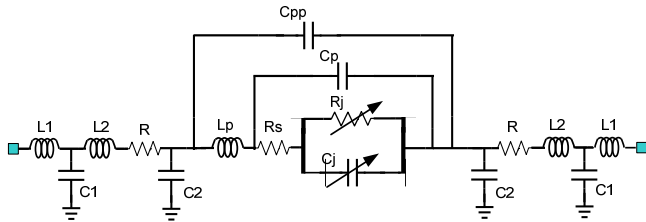

Fig.38. Lumped Equivalent Circuit for Schottky Diode with the Extrinsic Elements Detailed (Single Anode Diode)

The intrinsic device is represented through its characteristic elements: R_j is the nonlinear Schottky junction resistance that acts in parallel with the diode junction capacitance C_j, and the ohmic contact resistance is denoted by R_s. The equivalent values for each intrinsic element component are extracted from measured direct current (DC) characteristics and scattering parameters with fixed RF power levels ($\leq$ -30 dBm), and the diode unbiased and also reverse biased.

D. Results

S-parameter measurement data are compared with Schottky diode models in Agilent ADS with additional parasitic elements as shown in Fig.39. The target variables are extracted by performing curve fitting to the measured data. It should be noted here that our model takes into account the increase of the wire bonding series resistance caused by the skin effect at frequencies above 50 GHz and eventually by some other measurement uncertainties. In accordance with

the measurement equipment facilities at our laboratories, the measurements were carried out in two frequency ranges: DC-50 GHz and 75-110 GHz [35].
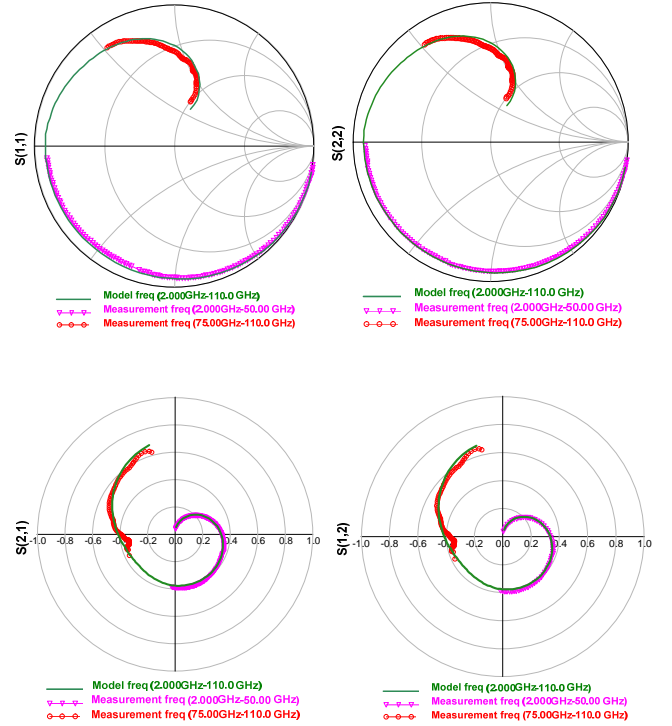

Fig.39. S-Parameter Simulation and Measurements for Schottky Diode using Diode Model (Fig.38). Diode is Unbiased (0V) – Single Anode

Parameters	Symbol	Value
Saturation Current(A)	I_{sat}	9.97593e-13
Ideality Factor	η	1.28
nkT/q (1/V)	α	30.31
Zero Junction Capacitance (Vd=0V) (fF)	C_{jo}	24
Series Resistance(Ω)	R_s	2.4429
Built in Potential (V)	Φ_{bi}	0.9
Finger Inductance (pH)	L_f	50
Parasitic Capacitance (fF)	C_p	1
Pad-to-Pad Capacitance (fF)	C_{pp}	15
Bonding Inductance (pH)	L_1	60.13
Bonding Inductance (pH)	L_2	51.36
Pad Capacitance (fF)	C_1	60.34
Pad Capacitance (fF)	C_2	46.26
Bonding Resistance (Ω)	R	0-3

Table 1.Extracted Parameters of the Schottky Diode under Consideration (Single Anode)

E. Other Types of Schottky Diodes

An antiparallel diode formed by two Schottky Single Diodes (see Fig.40) has been modeled following the previous equivalent circuit model, as it can be seen in Fig.38. In this model, a capacitance has been included to represent the effect existing between two fingers.
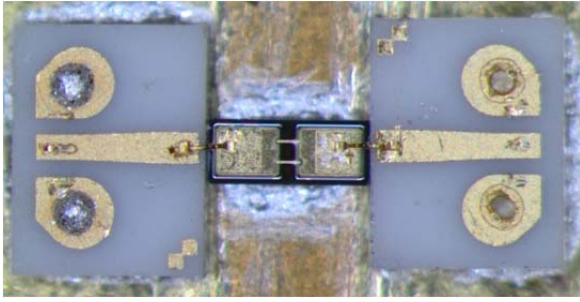
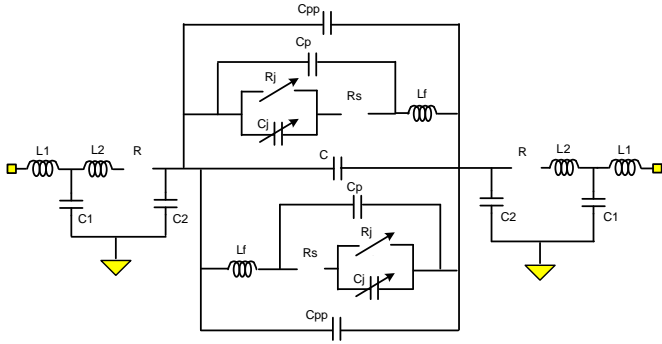Fig.40. Antiparallel Diode bonded with Gold Wires

Fig.41. Lumped Equivalent Circuit for Schottky Diode with the Extrinsic Elements Detailed (Antiparallel Diode)

The values of all elements in this lumped equivalent circuit model are shown in the table below:

Parameters	Symbol	Value
Saturation Current(A)	I_{sat}	$2.77492 \cdot 10^{-14}$
Ideality Factor	η	1.2543
nkT/q (1/V)	α	31.147
Zero Junction Capacitance (Vd=0V) (fF)	C_{j0}	16
Series Resistance(Ω)	R_s	2.2997
Built in Potential (V)	Φ_{bi}	0.9
Finger Inductance (pH)	L_f	50
Parasitic Capacitance (fF)	C_p	1
Pad-to-Pad Capacitance (fF)	C_{pp}	12
Bonding Inductance (pH)	L_1	70.13
Bonding Inductance (pH)	L_2	58.36
Pad Capacitance (fF)	C_1	52.34
Pad Capacitance (fF)	C_2	35.26
Bonding Resistance (Ω)	R	0-3
Capacitance between Fingers	C	105

Table 2. Extracted Parameters of the Schottky Diode under Consideration (Antiparallel Diode)

S-parameter measurements is compared with the antiparallel diode model (diode is unbiased). The simulations were carried out from DC up to 110GHz and the measurements in two frequency ranges: DC-50 GHz and 75-110 GHz (see Fig.39).
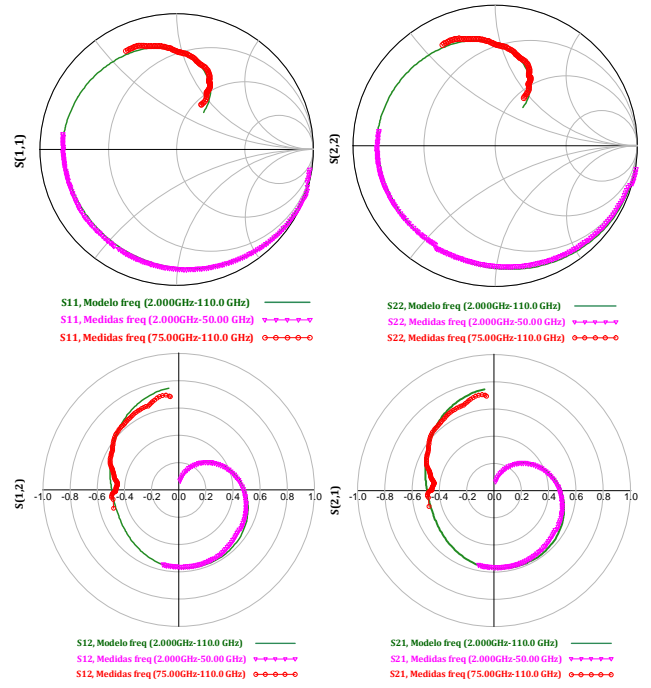

Fig.42. S-Parameter Simulation and Measurements for Schottky Diode using Diode Model (Fig.38). Diode is Unbiased (0V) – Antiparallel Diode

A third type of Schottky diode was modeled: the Zero Bias Diode (ZBD). This diode present the same equivalent circuit model that the Single Anode. Comparing the parasitics values of the ZBD (see Table 3) with respect to the Single Diode, an increase of parasitic capacitances in the edges of the diode pads is found due to its thinner substrate (55µm against 100µm).

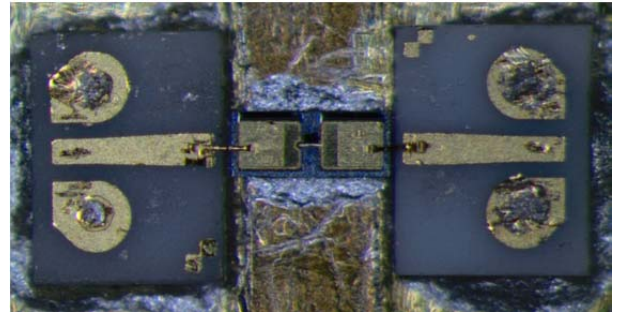Fig.43. Zero Bias Diode bonded with Gold Wires

Parameters	Symbol	Value
Saturation Current(A)	I_{sat}	$28.84738 \cdot 10^{-6}$
Ideality Factor	η	1.3669
nkT/q (1/V)	α	28.581909
Zero Junction Capacitance (Vd=0V) (fF)	C_{j0}	10
Series Resistance(Ω)	R_s	6.4760
Built in Potential (V)	Φ_{bi}	0.9
Finger Inductance (pH)	L_f	50
Parasitic Capacitance (fF)	C_p	1
Pad-to-Pad Capacitance (fF)	C_{pp}	16
Bonding Inductance (pH)	L_1	72.84
Bonding Inductance (pH)	L_2	41.77
Pad Capacitance (fF)	C_1	87.99
Pad Capacitance (fF)	C_2	50.57
Bonding Resistance (Ω)	R	0-3

Table 3. Extracted Parameters of the Schottky Diode under Consideration (Zero Bias Diode)

The S-parameters obtained in the simulation are excellently compared to the experimental measurements, as it can be seen in Fig. 34.
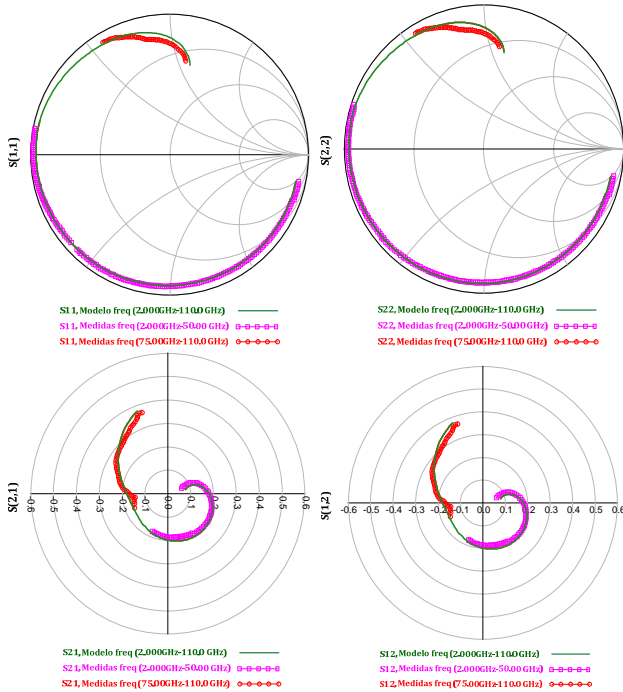

Fig.44. S-Parameter Simulation and Measurements for Schottky Diode using Diode Model (Fig.38). Diode is Unbiased (0V) – Zero Bias Diode

The parameters extracted from Zero Bias Diode provide an accurate RF model for nonlinear circuit simulations to design diode detectors. Therefore, this model has been used in the design of a detector as will be seen later in detail.
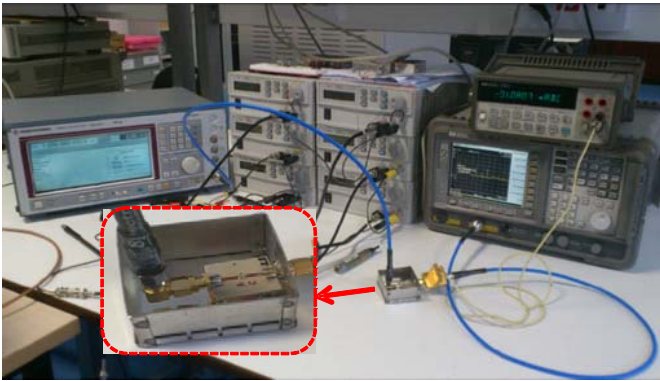

Fig.45. Setup for Low Frequency Pin vs. Pout Measurements

Additionally, a set up for low frequency P_{in} versus P_{out} measurements was done (see Fig.45), validating the capability of the models to fit measurements up to 3rd harmonic (see Fig.46).
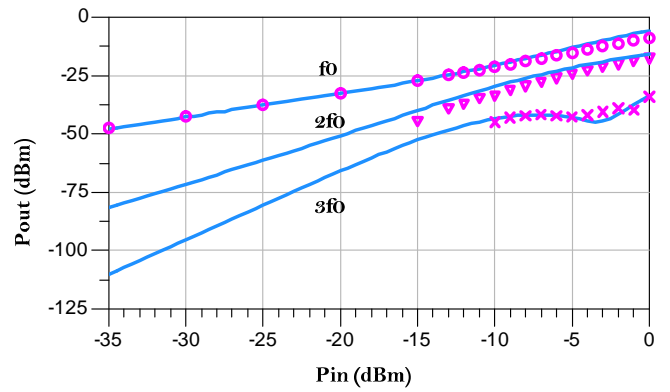

Fig.46. Fit Measurements up to 3^{td} Harmonic

The capability of our characterization and modeling method has been demonstrated to create a reliable equivalent circuit model of Schottky diodes with very good accuracy and valid under large signal conditions and at high frequencies up to 110 GHz. This was demonstrated using measurements up to 50 GHz and between 75 GHz and 110 GHz, although with a lack of measurements in the 50-75 GHz range. Using this model, the degree of agreement between measurements and simulations, for different diodes, validate the proposed approach.

IV. DESIGN OF MMICs

Some of the partners in TeraSense have a large background in design of MMICs and one of the goals of the project was to extend this experience to THz band, at least in the W band, to be able to provide added value in the MMICs design stage. Moreover, the use of, not Spanish, but at least European foundries was a strategic purpose. The list of foundries open to supply W band technology was very limited (IAF, OMMIC, UMS). Finally a set of MMICs own designed with European technology (OMMIC, France) was developed, but not yet manufactured due to limitations in budget (each prototype costs about 20.000€).

A single stage cascode LNA and a medium power amplifier have been designed with D007IH and D01MH OMMIC technology processes. Also a 4-stage LNA and a single dual balanced mixer are being designed, but they are not jet finished. This task has been developed by UNICAN.

A. Cascode Low Noise Amplifier (94-100 GHz)

The complete design of a Cascode Low Noise Amplifier (LNA) MMIC operating in a band between 94 and 100 GHz and based on microstrip technology using a process which employs 0.07 μm Metamorphic High Electron Mobility Transistors (D007IH OMMIC process), has been presented in [36]. A modified Cascode configuration combining resistive feedback and a lossy network to equalize gain and stabilize the circuit is used. The schematic diagram of the LNA is illustrated in Fig.47, where it can be seen with detail the structure of the design. The size of the transistors used is 4 x 15 μm.
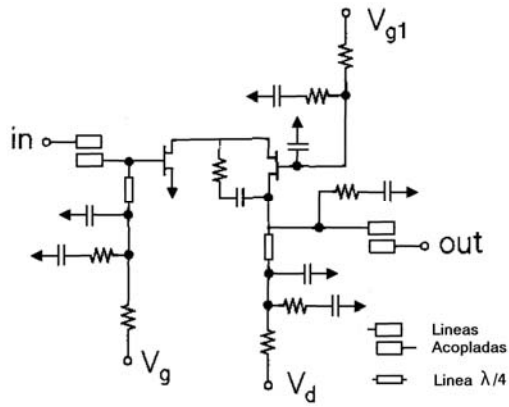
Fig.47. Schematic Diagram of the LNA

The layout of the final LNA which is prepared to be sent to OMMIC foundry is shown in Fig.48, where the free space of the dice has been used to place same transistors to be characterized in the future.
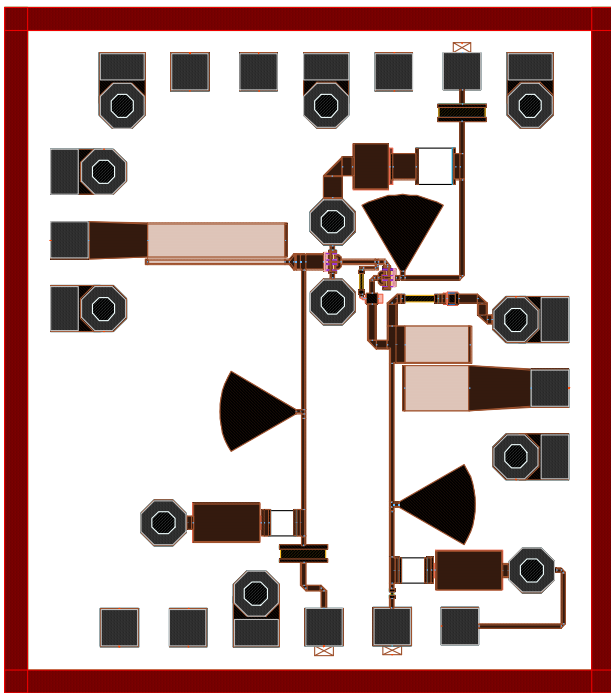

Fig.48. Layout of the LNA (1.5 x 1.335 mm^2)

The results obtained with the simulation based on the component models and the results obtained replacing the different passive networks of the design by their own S-parameters simulated in Momentum are presented and compared in Fig.49, Fig.50 and Fig.51.

In Fig.49, it is shown the small signal gain which is over 11 dB and the Noise Figure (NF) with a minimum value of 2.2 dB, being below 2.5 dB in the whole band.
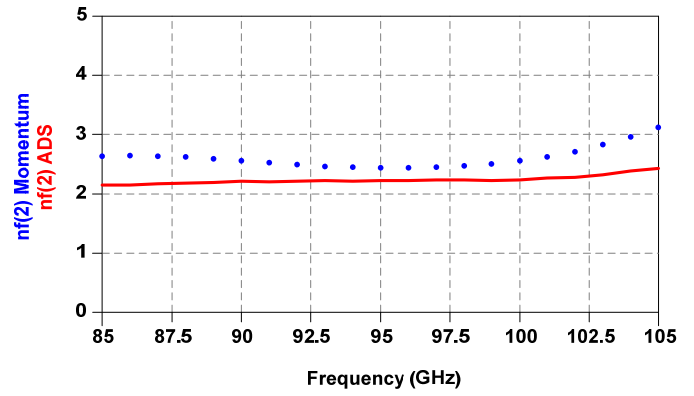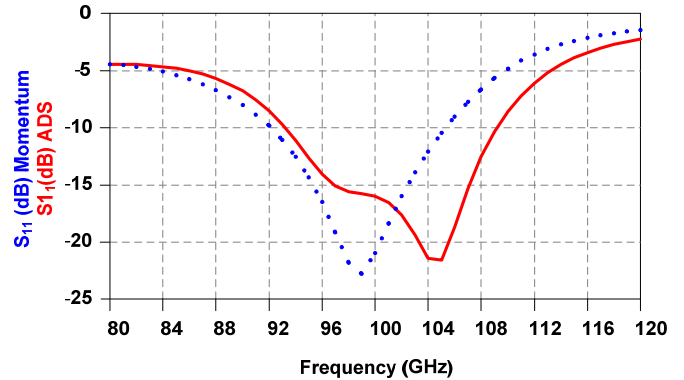

(a)
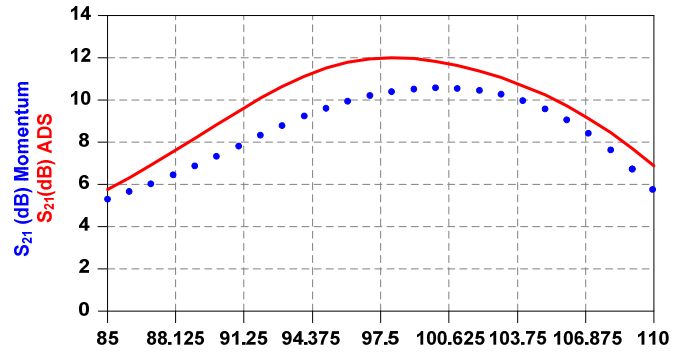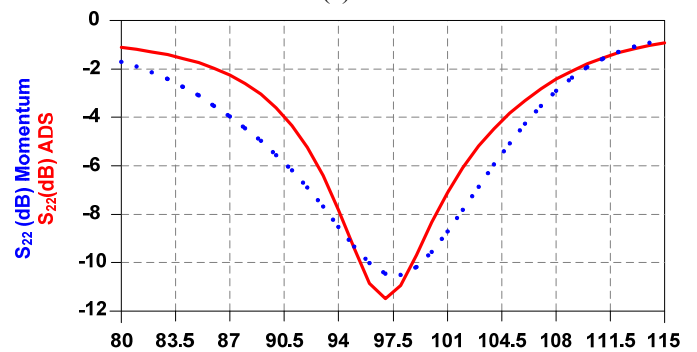

(b)

Fig.49. Noise Figure Results and Gain S^{21} of the Schematic Design (Solid Line) and Momentum (Dotted Line)

Regarding to the input and output matching, S$_{11}$ and S$_{22}$ are better than -15 dB and -8dB in the band of frequencies 94-100 GHz.

(a)

(b)

Fig.50. Input and Output Matching of the LNA Simulated in Schematic (Solid Line) and Momentum (Dotted Line)

The stability analysis parameter Mu has a value upper than 1 in the entire band where the model is valid, ensuring the unconditional stability of the LNA (see Fig.51).
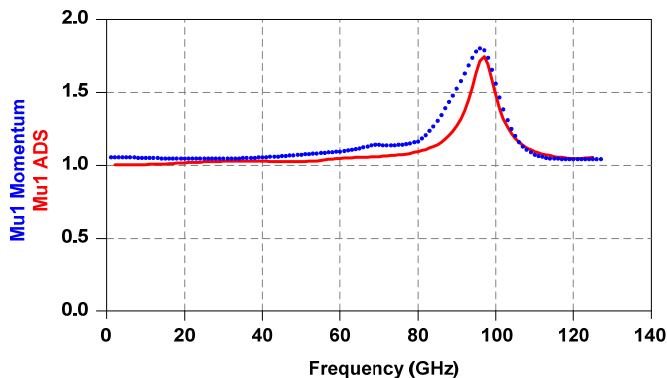

Fig.51. Stability Factor Parameter Mu>1: Unconditional Stability for all Frequencies

A summary of the principal parameters to take into account for a properly performance of the circuit design is shown in Table 4.

SYMBOL		MIN.	TYP.	MAX.
GAIN (dB)		11.2	11.7	11.9
REFLECTION COEFFICIENTS (dB)	S_{11}	-12.8		
	S_{22}	-9.7		
NOISE FIGURE (dB)				2.3
INPUT FREQUENCY (GHz)		94		100
VOLTAGE BIAS (V)	V_{G1}		-0.1	
	V_D		3.85	
	V_{G2}		1.4	
I_{SUPPLY} (TOTAL) (mA)			2.2	
P_{DC}(mW)			3.1	

Table 4. Summary of Fundamental Characteristics of LNA

B. A Three-Stage Medium Power Amplifier (94-100 GHz)

The design of a three-stage Medium Power Amplifier (MPA) MMIC operating in a band between 94 and 100 GHz has been explained in [37]. The amplifier circuit is based on a microstrip lines design with 0.13 µm gate length Metamorphic High Electron Mobility Transistors (D01MH OMMIC process). The schematic diagram of the LNA is illustrated in Fig.52, where it can be seen with detail the stages of the design. The size of the transistors used is 4 × 20 µm.
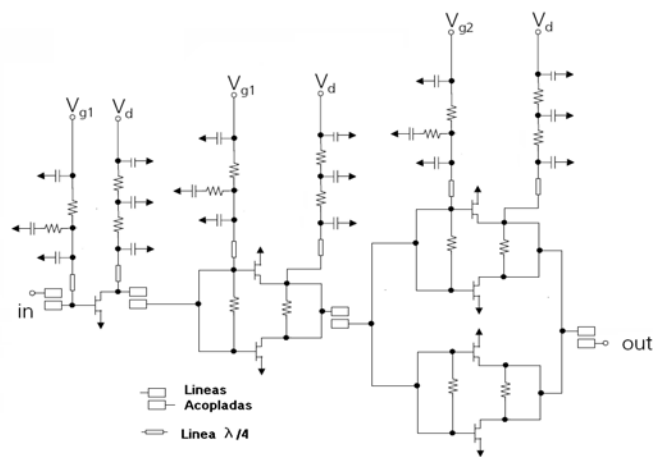
Fig.52. Schematic Diagram of the MPA

The layout of the final LNA which is prepared to be sent to OMMIC foundry is shown in Fig.53, where the free space of the dice has been used to place same transistors to be characterized.
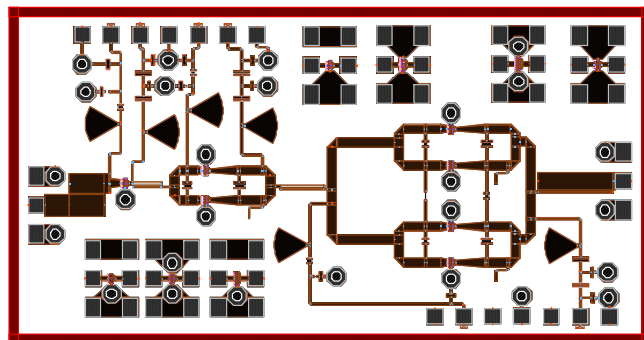
Fig.53. Layout of the MPA (1.743 x 3.314 mm^2)

Simulations have been carried out with the non lineal complete model of MHEMT transistors to describe their behavior in large signal. DC bias chosen was: V_{gs1}=-0.05 V, V_{gs2}=-0.15 V and V_{ds}=4 V, obtaining a reasonable gain in spite of limiting the reached efficiency. The Pin-Pout curve has been simulated at a central frequency given in the band, obtaining the gain in available power (see Fig.54). The 1dB compression point is placed in P_{out1dB}= 13.12 dBm for P_{in}= 2.6 dBm.
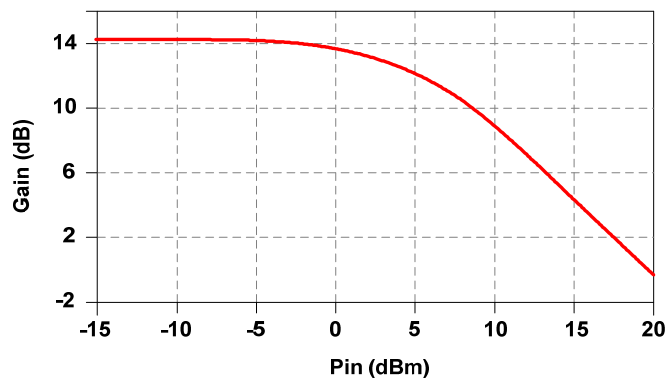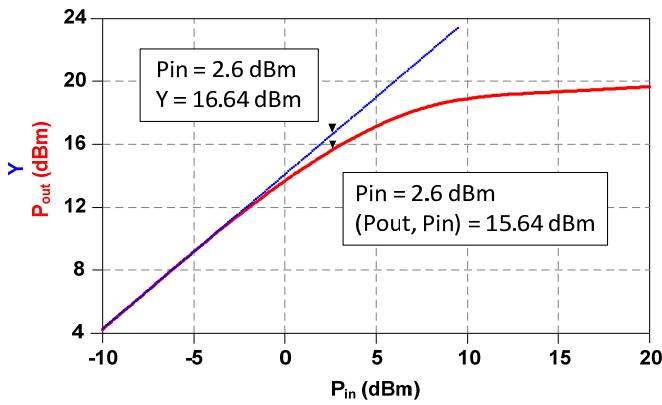
Fig.54. Gain Curve and Pin / Pout at 97 GHz

The Power Added Efficiency (PAE) has been evaluated too, reaching values above 10%. PAE is plotted in Fig.55.

Fig.55. PAE as a Function of P_{in}

The behavior in function of the frequency has been evaluated using large signal S-parameters, which considering the injected power level in the amplifier and let show the compression of the gain. In the Fig.56, the gain as a function of frequency for a wide range of input power is plotted. It can be seen the gain curves progressively compressed from 4dBm of input power.
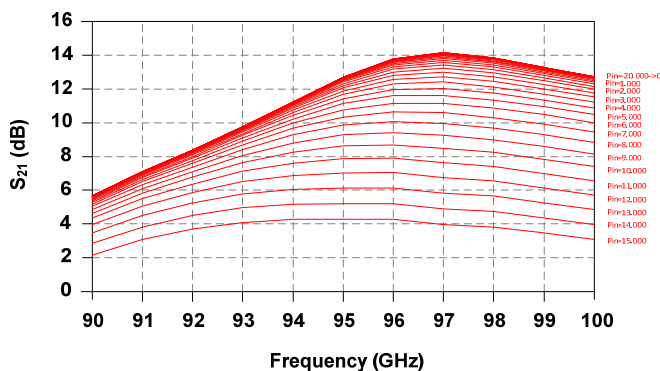
Fig.56. Gain as a Function of Frequency varying P_{in} from (-20dBm to 15dBm) using Large-Signal S-Parameters Analysis

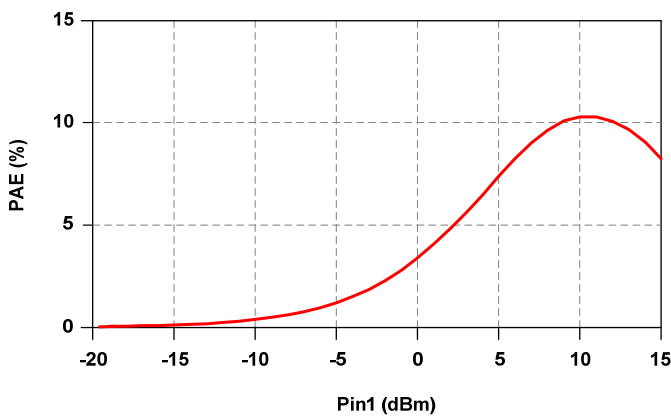In Fig.57, the input matching is shown, where the compression can be seen as deterioration of the values, and in Fig. 58, the output matching is shown which is less sensitive to the input power.
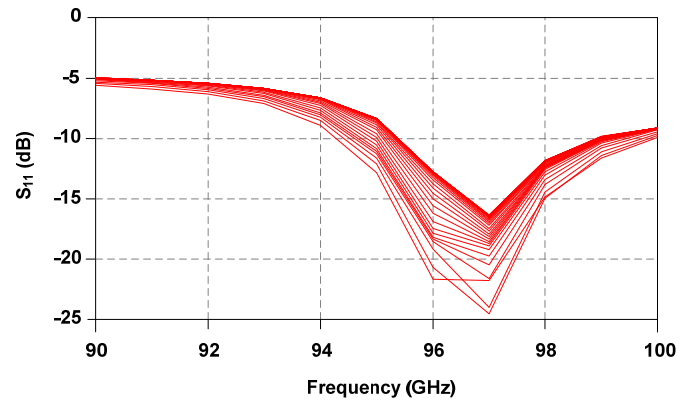
Fig.57. S_{11} (dB) in Large Signals function of Frequency varying P_{in} from (-20dBm to 15dBm)
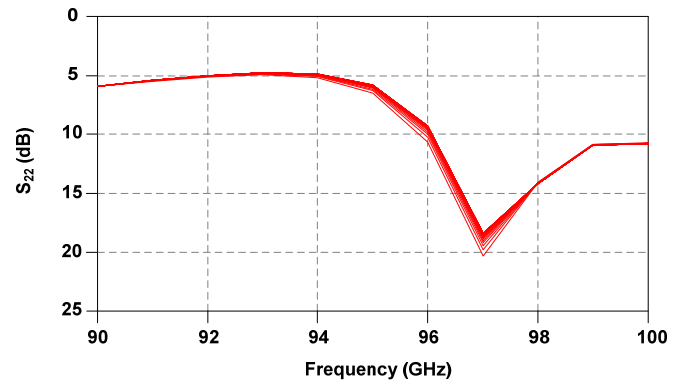
Fig.58. S_{22} (dB) in Large Signals function of Frequency varying P_{in} from (-20dBm to 15dBm)

A summary of the principal parameters to take into account for a properly performance definition of the designed circuit is shown in Table 5.

SYMBOL		MIN.	TYP.	MAX.
GAIN (dB)		11.25	13.3	14.15
REFLECTION COEFFICIENTS (dB)	S_{11}	-7.9		
	S_{22}	-4.5		
INPUT FREQUENCY (GHz)		94		100
OUTPUT POWER(1dB) @ 97 GHz (dBm)			15.5	
VOLTAGE BIAS (V)	V_{G1}		0	
	V_D		3.5	
	V_{G2}		0	
	V_{G3}		-0.2	
I_{SUPPLY} (TOTAL) (mA)			213.0	
PAE (%)				8.9

Table 5.Summary of Fundamental Characteristics of MPA

V. ON WAFER CHARACTERIZATION OF COMMERCIALLY AVAILABLE MMICS

There is a very limited list of suitable MMIC circuits commercially available, most of them manufactured in USA and available with restrictions. One of the most interesting suppliers is Hughes Research Labs (HRL) which fabricates W band LNAs with 4 and 5 stages, Medium power amplifiers and detectors.

Those devices could be acquired as a dice or eventually already connectorized. The former option retains some added value but requires facilities, first for measuring and characterization and later for assembling.

This task has been developed by UNICAN. Facilities available for on wafer testing were: Vectorial Network Analyzer in W band (PNAX + W heads) + probe station Cascade Summit + Picoprobe probes 125 µm pitch (Fig.59).
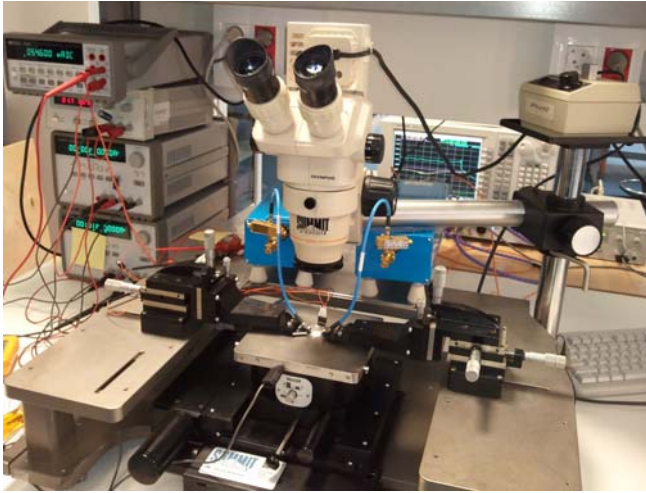
Fig.59. Laboratory Set-up for on Wafer Measurements of MMICs

The first measurements of the available MMICs are done on wafer [39] in order to verify the specifications provided by the manufacturer. On the one hand, the 5-stages LNA (LN5-100) with its DC biasing network formed by different values of capacitors and resistances (10Ω for drain and 1KΩ for gates) is shown in Fig.60.
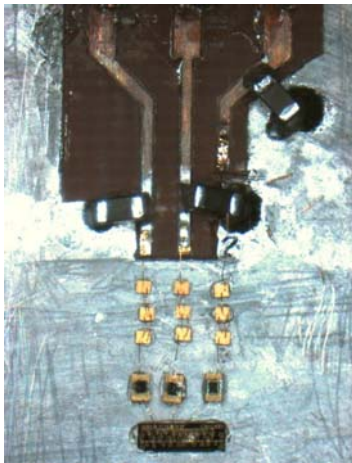
Fig.60. LN5-100 on Wafer Assembly

The four S-parameters measured are shown in Fig.61. A constant gain from 75 up to 102 GHz (working range of this LNA) with a maximum value about 16 dB (below the desired value of 29 dB which is the provided gain by the manufacturer) has been measured. This can be due to an unwanted oscillation or a possible damaged stage.
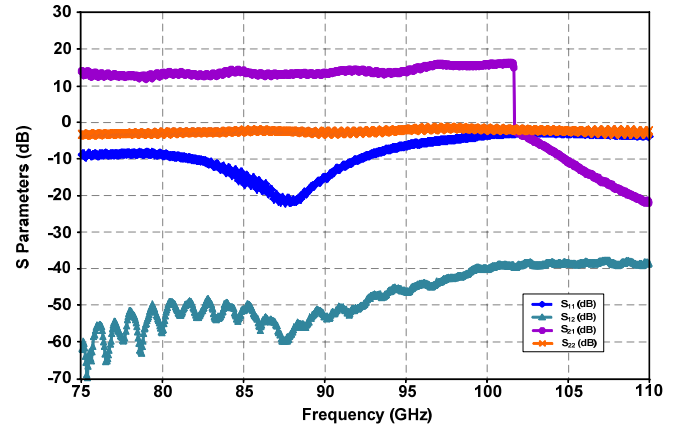
Fig.61. S-parameters measured of LN5-100 (HRL)

On the other hand, the 4-stage LNA (LN4-110) shown in Fig.62 has been assembled with the same type of biasing networks as the previous LNA and the S-parameters measured are shown in Fig.63.
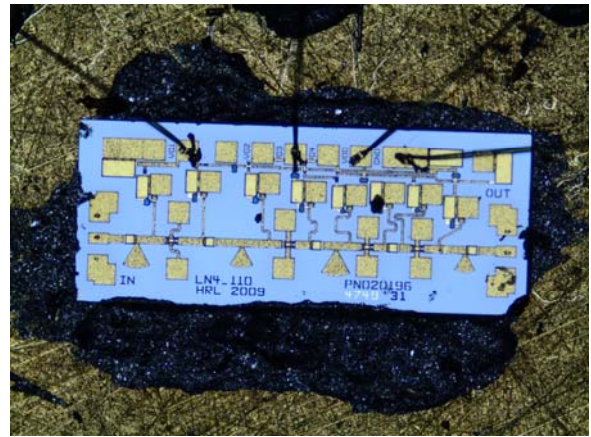
Fig.62. LN4-110 on Wafer Assembly

In this LNA, the gain has a constant behavior in the entire range, but in this case, with a maximum value around 20 dB, higher than the LN5-100 gain and much more similar to the expected response (24 dB is the value given by the manufacturer). Furthermore, this LNA operates in the entire W band (form 75 up to 110 GHz), therefore LN4-110 has been chosen for the future radiometer because seems more stable and reliable than the 5-stage LNA. If it were necessary to obtain a higher sensitivity with a suitable level of gain, it could be possible to cascade two LN4-110.
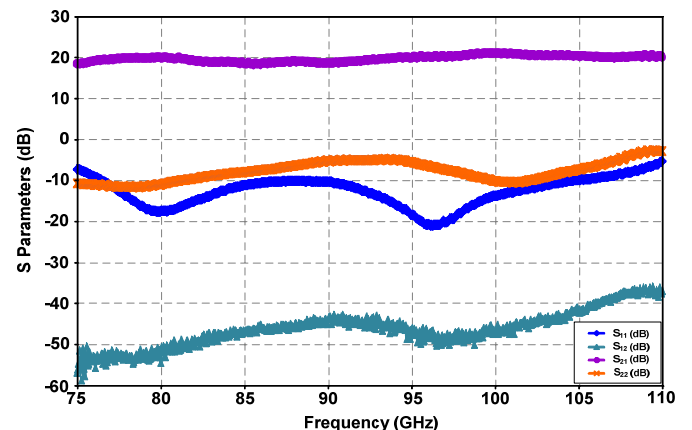
Fig.63. S-Parameters measured of LN4-110 (HRL)

The diode-detector V1A MMIC presents a high sensitivity given by the manufacturer about 15.000 mV/mW at 95 GHz.

The laboratory setup has been the same for the LNAs measurements using the PNA-X and the probe station with Picoprobe probes 125 μm pitch, but in this case, the output of the set-up has been connected to a multimeter to detect the output DC voltage. A -30dBm input power signal is applied to obtain an adequate response (value recommended in the datasheet). From the Fig.64, it can be seen that this detector is more sensitive in the range 85-95GHz, obtaining higher values of output voltage.
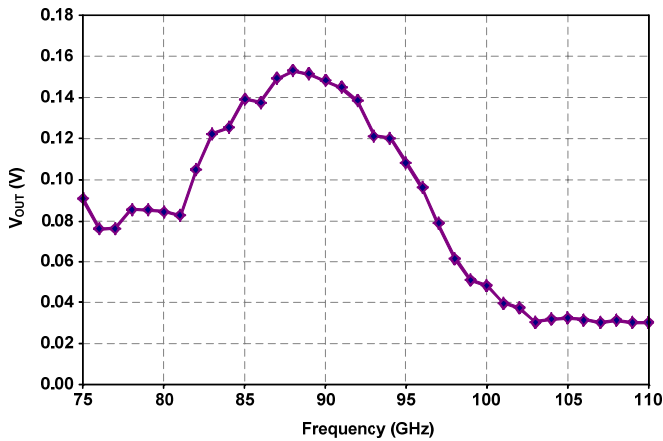
Fig.64. Output Voltage (V) of the V1A for a Frequency Sweep at a Fixed Input Power

Keeping in mind the goal of the W band receiver development [38], an on-wafer total power radiometer was formed by connecting the 4-stage LNA MMIC with the detector MMIC using wire bonding. RF input pad of the LNA and DC output pad of detector were left unconnected, to place the probes on them (Fig.65 and Fig.66).
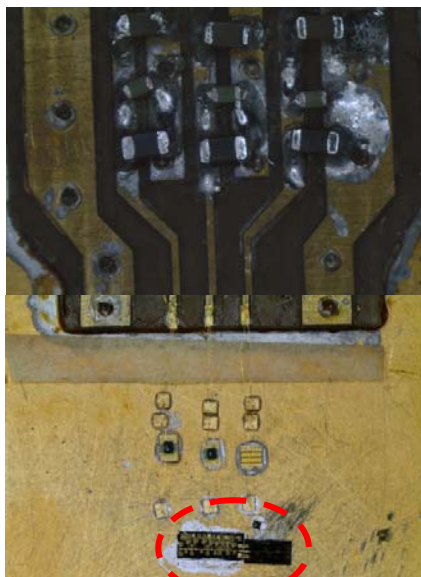
Fig.65. On Wafer Assembly of the Total Power Radiometer (LN4-110+V1A)
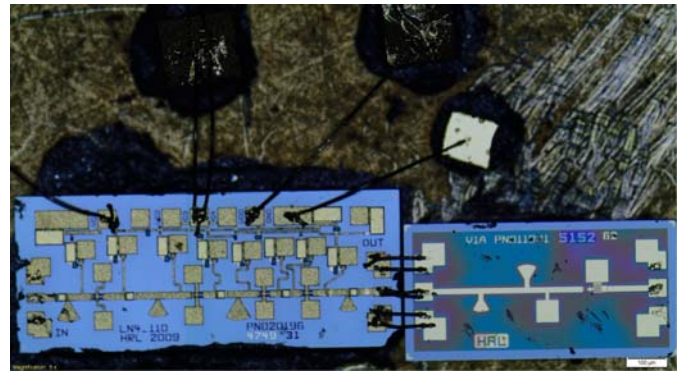
Fig.66. Zoom of the Total Power Radiometer Assembly

Taking into account that the input power level in the detector is -30dBm and that the LN4-110 gain is about 20dB, the input power level of the total power radiometer should be a value of approximately -50dBm. The results obtained are shown in Fig.67, where we can see a response similar to the single detector assembly.
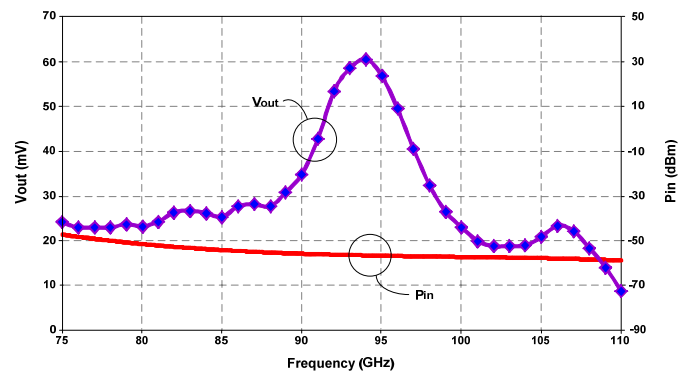
Fig.67. Output Voltage (mV) of the LN4-110+V1A for a Frequency Sweep and Input Power (dBm)

Following the same DC biasing scheme of LNAs assembly, a medium power amplifier (LSPA2) has been mounted to perform on wafer measurements for characterizing it (see Fig.68 and Fig.69).
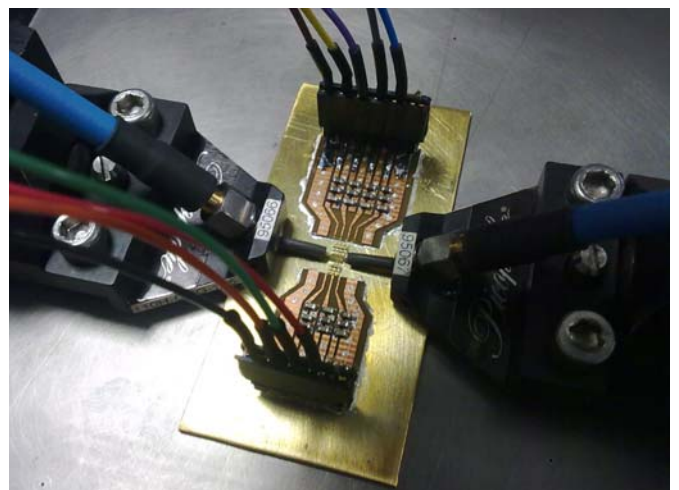
Fig.68. LSPA2 on Wafer Assembly with Coplanar Probes positioned over Input and Output Pads
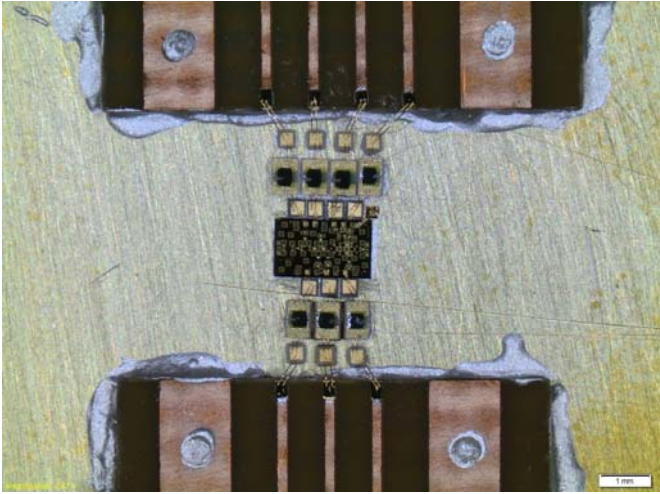
Fig.69. Zoom of the LSPA2 on Wafer Assembly

Fig.71. Pin-Pout Curves at 94GHz and 97GHz of LSPA2 (HRL)

The four S-parameters are measured with an input power about -30dBm obtaining a quite stable response, as it can see in Fig.70.

Fig.70. S-Parameters measured of LSPA2 (HRL)

The typical P_{in}-P_{out} curve is also represented from the measurements realized in the laboratory at two different frequencies of interest: 94GHz and 97GHz. It is interesting to note that these curves have been corrected taking into account the losses of the setup elements (waveguide-to-coaxial transition, 1mm-coaxial cables and coplanar probes losses). From the datasheet of the medium power amplifier, it is known that the maximum rating for the input power is 10dBm, but the curves are obtained only up to -10dBm, due to the impossibility for obtaining an input power greater than this value with the available instrumentation equipment. From these results, we can conclude that the LSPA2 comprises beyond, at least, -10dBm.

VI. DEVELOPMENT OF SPECIFIC MECHANICAL STRUCTURES AND MICROSTRIP HYBRID BOARDS FOR ASSEMBLING OF SYSTEMS

All of the partners had previous experience and background in developments reaching the high part of the microwave spectra (Q, V, etc.) but, for most of them, TeraSense meant a challenge for a further jump to W and G band. This increase in frequency means a decrease in size, therefore pushing the manufacturing facilities to the limits of accuracy and precision.

Lowest losses in the connection of system parts are provided by waveguides, compared to coaxial cables, but on the other hand a microstrip line environment seems more suitable for assembling MMICs and hybrids circuits. Therefore the development of waveguide-to-microst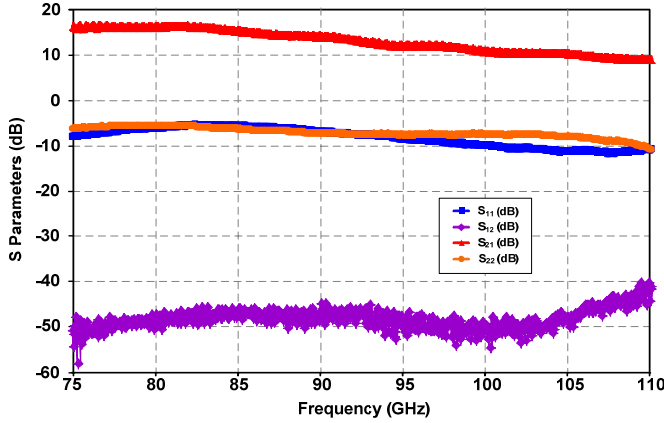rip transitions becomes a primary requirement (section A). For some applications, like characterization of dielectric materials, quasi-optical configurations avoiding connectivity restrictions may be used. In section B, a Quasi-optical Measurement System in W band for characterization of materials is presented. In section C, an 80GHz Medium power amplifier assembling in WR10 waveguide is shown. Section D shows the design and measurements of a band pass filter in W band. In section E a study about optimum feasible coplanar to microstrip transitions is presented. In section F, the design of a WR10 waveguide assembling of LNAs and LNA+detector in W band is shown. Finally, in Section G, W-band Noise Figure Measurements of LNAs are presented.

A. W-Band E-Plane Waveguide-to-Microstrip Transitions

This task has been developed by UNICAN. Regarding the robustness of the prototype, longitudinal E-plane transitions seem more suitable than other type of transitions to obtain the maximum transmitted signal. The waveguide-to-microstrip transition is composed of a standard W-band waveguide, WR-10, and a cut-off cavity which contains the required microstrip line and the strip transition entering the waveguide. This microstrip section is composed of the probe which captures the signal from the input WR-10 waveguide, a section of high-impedance microstrip line to compensate the impedance value for the capacitive reactance that the probe introduces, a quarter-wave impedance transformer to transform the impedance obtained at the end of this high-

impedance line to the desired 50 Ω level and finally, a section of 50 Ω microstrip line.

Two of these structures have been optimized and connected to constitute a back-to-back transition necessary to measure the available circuits in the laboratory.

A thin substrate thickness is essential in W band to avoid unwanted propagation modes. A value of 5 mils or even lower thickness is considered suitable. A trade-off between low cost, flexibility, size and performance was required. Two versions, with RT/Duroid 5880 and with ULTRALAM 2000 have been used for the design and fabrication of the circuits.

A.1. RT/Duroid 5880 Substrate

This substrate is used for the waveguide-to-microstrip transition necessary for assembling of the available commercial MMICs. It has the following characteristics: h = 5mils, ε_r=2.2 and tanδ=0.0009 @ 10GHz.The design of the back-to-back transition can be seen in detail in [40], [41] and it is shown in Fig.72.
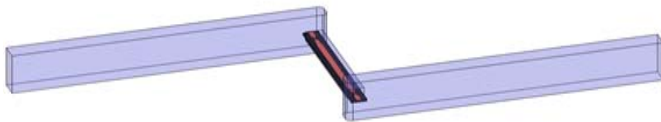
Fig.72. The Back-to-Back Transition in W Band

The accuracy of the fabrication process is crucial for obtaining good experimental results. Several prototypes of the transition have been fabricated and measured with a high-resolution microscope, and the most similar to the nominal dimensions of the design has been selected. Furthermore, a good tolerance (±20μm in the dimensions according to the manufacturer) was required too for the brass mechanized box (Fig.73).

Fig.73. Photographs of the Metal Case for the Back-to-Back Transition (4 × 3 × 2.4 cm^3)

Finally, assembly of the microstrip lines on the metal case was done, as is depicted in Fig.74. To attach the microstrip lines to the structure we have used solder and it has been necessary to be careful with the positioning of the microstrip lines into the cut-off cavity.

(a)   (b)
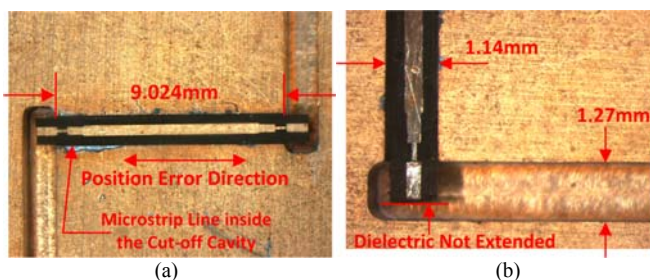
Fig.74. The Final Assembly (Microstrip Lines inside the Metal Case). (a) View of the Complete Microstrip Section. (b) Detail

The simulated S-parameters results are compared with respect to the obtained experimental measurements and they are shown in Fig.75.
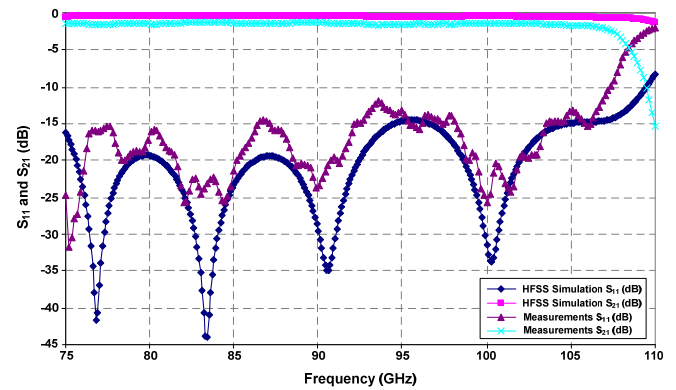
Fig.75. A Comparison between the Measurements obtained and the Previous Simulation

Actual deviations from nominal dimensions in microstrip lines, displacement in their positioning and the effect of the gilding process of the microstrip line were included into the 3D EM simulator. This simulation reproduces more accurately the fabricated transition. Comparison with the measurements is shown in the Fig.76, concluding that the agreement between measurements and simulation has improved. Differences between simulated and measured S_{21} may be related to the metal losses.
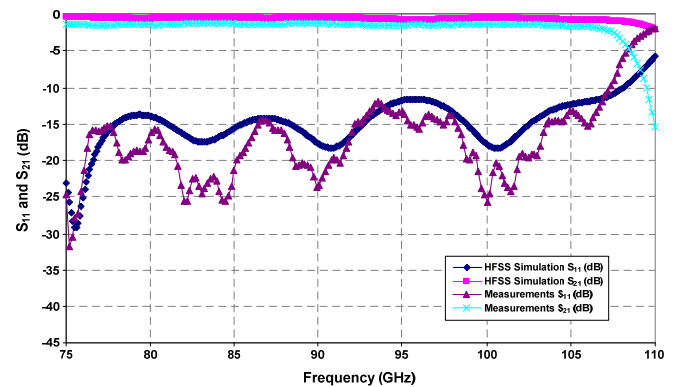
Fig.76. A Comparison between Measurements and a more Realistic Simulation taking into account Fabricated Dimensions

A.2. Ultralam 2000 Substrate

This substrate, as it was said in subsection II.A, has been chosen for the design of the linear array of planar antennas feed by slots [12]. ULTRALAM 2000 has the next characteristics: h = 4mils, ε_r= 2.5 and tanδ = 0.0019. The steps carried out during this design are identical to the previous transition and the comparison between simulated S-parameters and the measurements obtained in the laboratory can be seen in Fig.77.
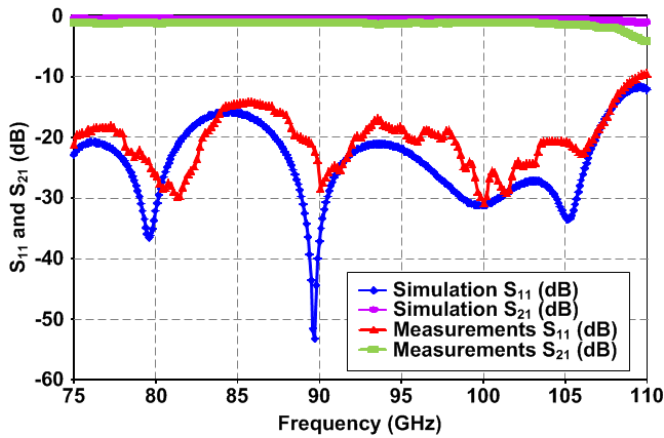
Fig.77. Simulation and Experimental Results of the Back-to-Back Transition in W-band

A double waveguide-to-microstrip transition (back-to-back transition) has been fabricated to check the validity of the design, although in the design of the array is only necessary a single transition.

B. W-Band Quasi-Optical Measurement System

The accurate knowledge of the properties of dielectric materials, such as those used to manufacture substrates, radomes, or lens antennas, is essential to carry out the design of devices and circuits in the millimeter wave (MMW) range. The knowledge of the material properties can also be used in MMW scene simulators that render photorealistic images that allow one to predict if certain objects (i.e. metals, explosives...) can be identified within a scene for a given atmospheric effects, noise, blur or imaging system parameters [42], [43]. This task has been developed by UAB.

In the W-band (75 – 110 GHz), a quasi-optical measurement system [44] is an attractive alternative to measure these properties since it is contactless, non-destructive and the sample preparation is easy. Furthermore, broadband characterization can be achieved.

B.1. Measurement System Description

The designed measurement system is shown in Fig.78. It consists of an input beam waist at the aperture of a feed horn that is refocused or collimated by an off-axis parabolic mirror to form an output beam waist at the sample position. The transmitted beam is passed, via another off-axis parabolic mirror to a second horn that feeds the receiver.

Unlike [44], we use reflective focusing elements instead of lenses. Reflective focusing elements are free from the absorptive and reflective losses that characterize refractive focusing elements. In order to keep cross-polarized radiation and distortion low it is convenient to have an effective focal length (f) larger than the aperture diameter (D_a) [45]. Therefore, we choose a commercial mirror of Janostech [46] with f = 152 mm and D_a = 101.6 mm.

A smooth-walled spline-profile horn [47] has been used as an alternative to a corrugated horn. The length of this horn (70 mm) is somewhat larger than a corrugated horn (40 mm) but it provides similar results with significant improvements in ease of manufacture.
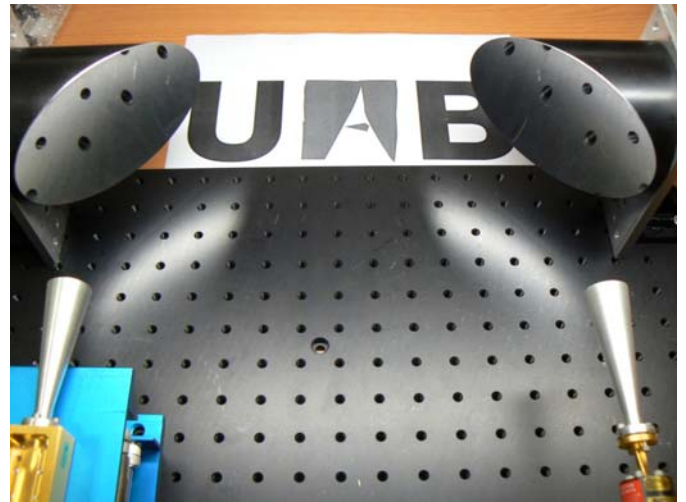
Fig.78. Quasi-Optical Measurement System

B.2. Simulations and Experimental Validation

The proposed quasi-optical system through was validated through simulations using the physical optics (PO) implementation of FEKO [48].

In Fig.79 we have depicted the near field in the plane defined by wave propagation. Indeed the input beam waist at the aperture of the feed horn is refocused at the sample while the radiation is largely collimated, thus keeping spill-over losses low.
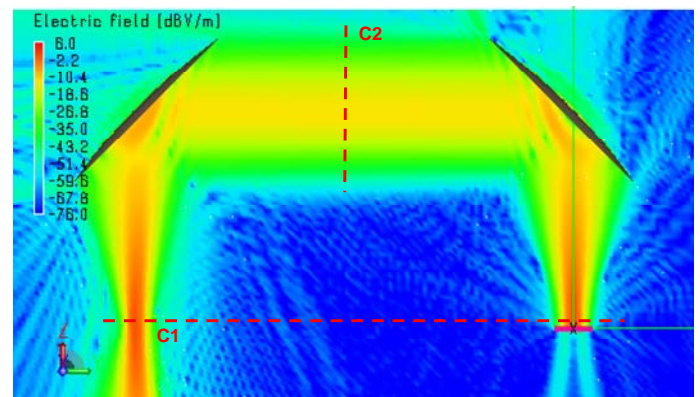
Fig.79. Near Field generated by the proposed Quasi-Optical Measurement System at 94 GHz

The near field along the cut C1 is plotted in Fig.80. It can be seen that input Gaussian beam is recovered without appreciable losses. The computed gaussianity of the beam at C2 is 99.5% thus we can assume that a plane wave is obtained at the sample plane as predicted.
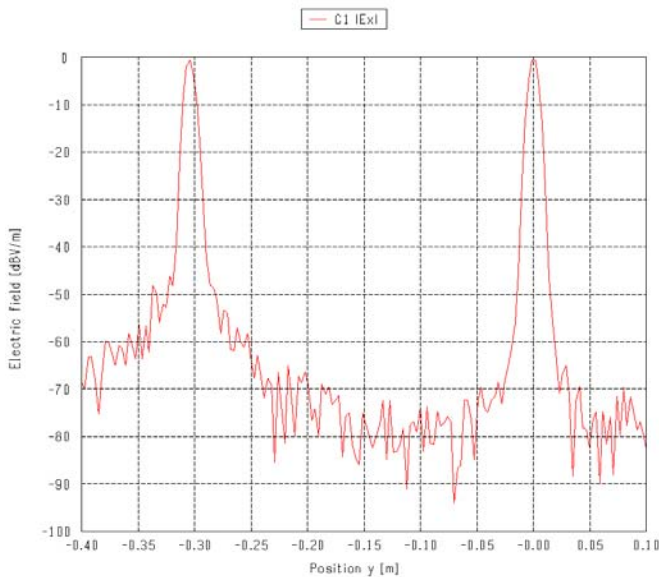
Fig.80. Near Field along C1. The Input Gaussian Beam is recovered without Noticeable Losses

The measured system efficiency is around 80% in the entire W-band. This efficiency includes losses in the free space path, horns and waveguide transitions.

The proposed setup has also been used in order to characterize a homemade teflon lens. Measurements and simulations (Fig.81) show an excellent agreement.
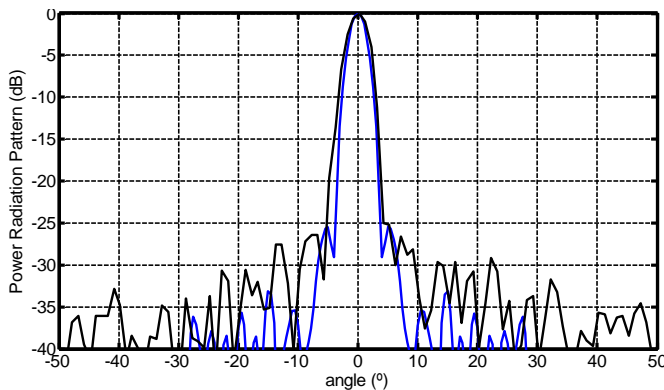
Fig.81. Characterization of a Zone Plate Lens

C. 80 GHz Medium Power amplifier

This task has been developed by UPC. An 80 GHz medium power amplifier MMIC Hittite AUH-320 has been mounted using two finline waveguide to microstrip transitions. The components have been placed on a brass mechanized box where both the input and the output of the box are WR-10 waveguides. Fig.82 shows the finline transition placed on the channel of one half of the box.
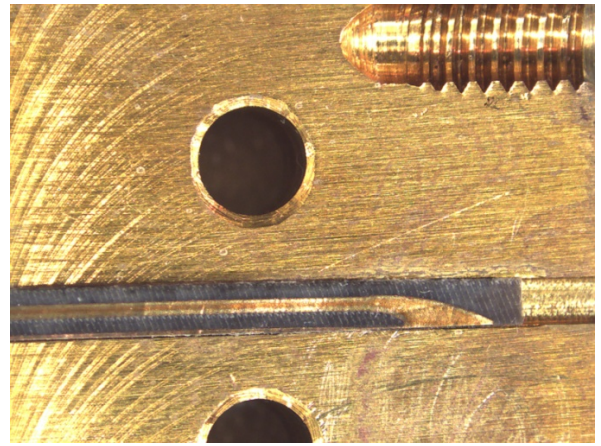
Fig.82. Finline Transition placed on half of the WR-10 Waveguide

The MMIC has been fixed to the box channel using conductive epoxy to have a ground contact with the box. The connections to the finline transitions and to the DC bias have been performed using thermo-compression wire bonding. Fig.83 shows a photograph of the MMIC placed on the box channel. The upper part of the image shows the bias circuitry connected to the MMIC by wire bonding.
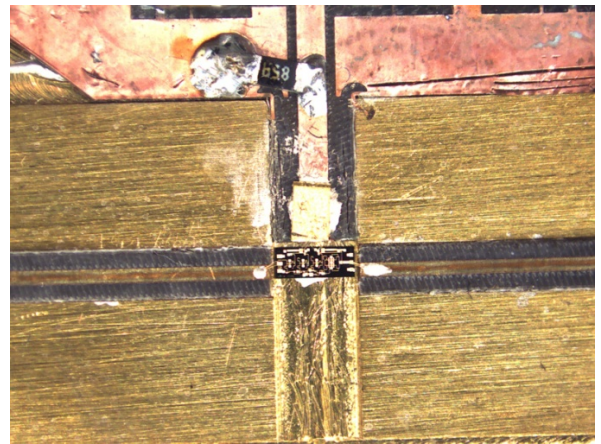
Fig.83. Amplifier MMIC placed on the Box. Both Finline Transitions as well as the DC Biasing are connected by Wire Bonding

The amplifier gain and return loss have been measured from 74 GHz to 86 GHz. Fig.84 shows the measured gain of the amplifier. A maximum gain of 16 dB is obtained at 78 GHz, agreeing with the specifications provided by the manufacturer. Additionally, Fig.85 shows the measured return loss of the amplifier showing a good matching from 78 GHz to 83 GHz.
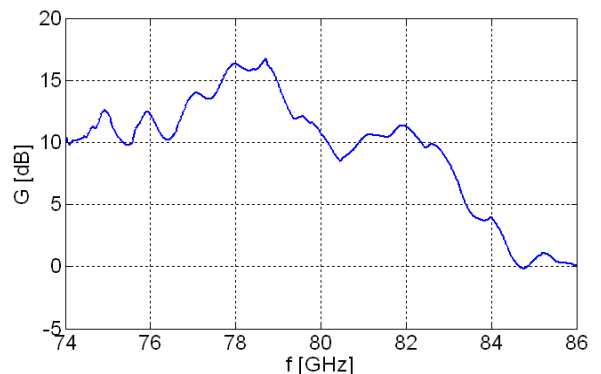
Fig.84. Measured Gain of the Amplifier

Fig.85. Return Loss of the Amplifier

Fig.87. Simulation and Experimental Results of the Band Pass Filter in W-band
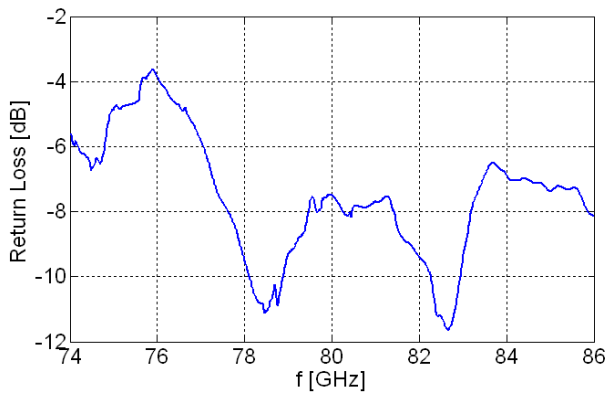
D. Band pass Filter

This task has been developed by UNICAN. Five-stages coupled microstrip band pass filters in W band have been designed and manufactured in 5 mils thickness substrate (RT/Duroid 5880). The objective of this filter is to define the 6 GHz-bandwidth (from 94GHz up to 100GHz) shape of a total power radiometer design.

This band pass filter is connected with the same model of coplanar-to-microstrip transitions (model PROBE POINT TM0503 transition) used in diode characterization [31], and bonded with gold wires with a diameter of 17μm in order to enable on-wafer measurements using air coplanar probes. The complete assembly fixed with conductive epoxy can be seen in Fig.86.
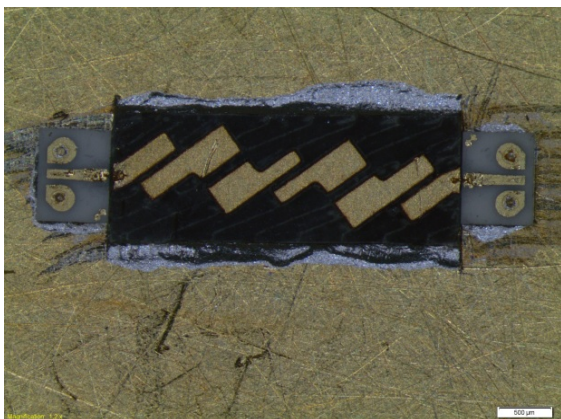
Fig.86. Assembly of the Band Pass Filter in W-band

Comparing simulation results and on-wafer experimental measurements (see Fig.87), around 6dB of difference in losses (S_{21} parameter) can be seen. This may be due to the coplanar-to-microstrip transitions and gold wires losses. A more similar matching has been obtained (S_{11} parameter).

Finally, the use of this filter has been discarded in the assembly of the total power radiometer in order to maximize the bandwidth and sensitivity of the own radiometer. This decision was taken from the comparison of several simulations of the complete system radiometer [49], [39].

E. Coplanar-to-Microstrip Transitions Study

This task has been developed by UNICAN. Flip chip mounting is preferred (i.e. for diodes), but if wire bonds are unavoidable, (MMICs) coplanar-to-microstrip transitions should be carefully designed to minimized mismatching and degradation of on-wafer response. Those reasons drove us to a comparative study with simulations and measurements of different transitions affordable by our manufacturing facilities.

In first place, a commercial coplanar-to-microstrip transition is modeled to be used in future designs such as the next assembly which will be shown later and for the design of a home-made detector based in Schottky diode. For this, an assembly with two transitions and a gold bonding wire which connects two transitions is mounted (see Fig.88).
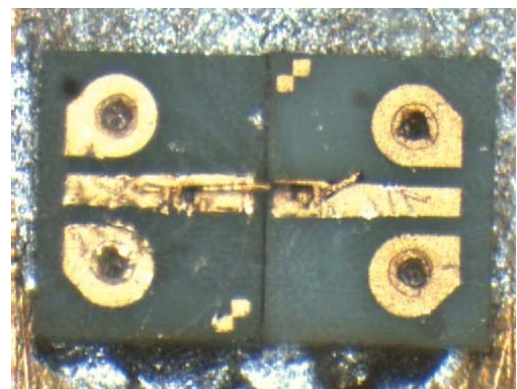
Fig.88. Assembly of Two Coplanar-to-Microstrip Transitions connected with a Gold Bonding Wire (Thickness Substrate 5 mils)

The coplanar-to-microstrip transition has been modeled in two ways. On one hand, through an equivalent circuit model composed by microstrip and coplanar sections [32] using ADS and on the other hand, through a 3D electromagnetic model using HFSS. This last model is more accurate than the previous one, therefore, will be used for future designs with need it. The same assembly composed of two transitions and the gold bonding wire is designed (see Fig.89) and simulated

with HFSS to be able to compare the S-parameter simulation results with S-parameter measurement results.
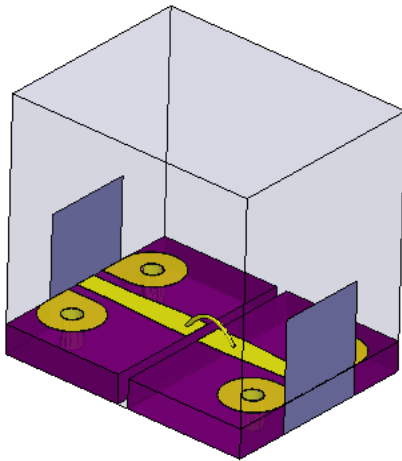
Fig.89. 3D Viewof the HFSS Electromagnetic Model of the Two 5 mils Transitions with Gold Bonding Wire

Experimental measurements have been done using a PNA analyzer with the coplanar probes station for the DC-50GHz frequency range and the PNA-X analyzer + W-band external modules with the coplanar probes station for W-band frequencies (75GHz up to 110GHz).
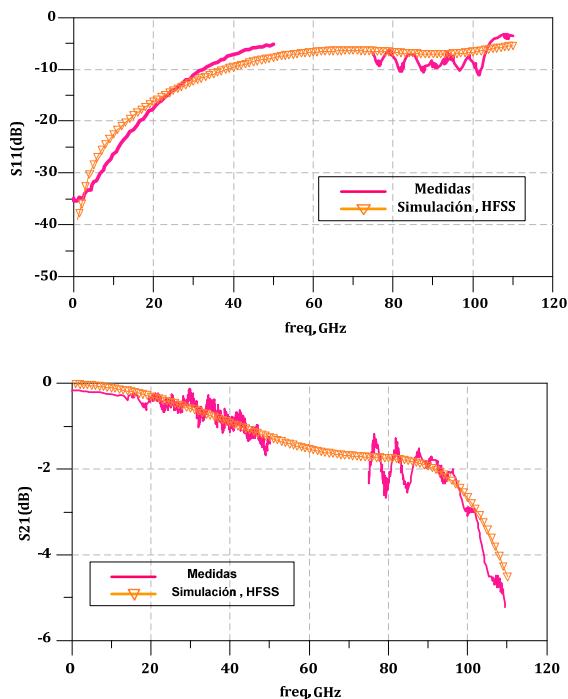
Fig.90. Comparison between S-Parameters of EM Simulation Results and Experimental Measurements of the Assembly

The comparison between simulations in the entire frequency range and two experimental measurement results (S_{11} and S_{21} parameters) can be seen in Fig.90. A good agreement is obtained between both results, obtaining the valid model in the whole frequency range.

Other type of home-made coplanar-to-microstrip transitions could be necessary for some assemblies. So, the assembly of MMICs into a metal case housing needs the waveguide-to-microstrip transitions previously shown in subsection IV.A, both for input and output. Moreover, the own termination of this transition uses microstrip technology

and the MMICs presents coplanar inputs and outputs, therefore coplanar-to-microstrip transitions are necessary in these assemblies.
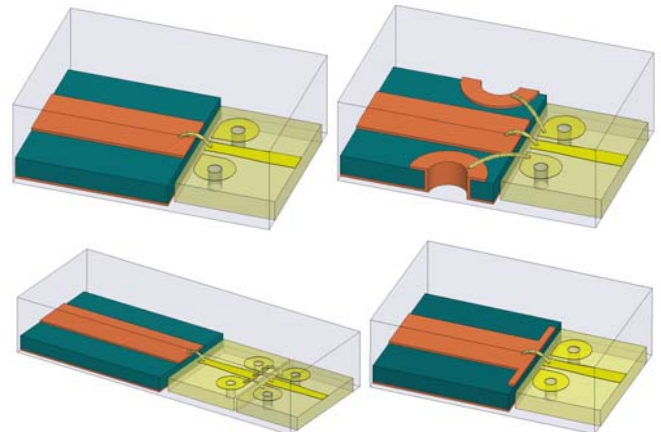
Fig.91. Different Options for the Monolithics Connections

A coplanar-to-microstrip transition (model PROBE POINT TM0503 transition) has been used in the simulation instead of the MMIC coplanar input since it also presents coplanar technology. In four configurations simulated (see Fig.91) [39], the common part in the design is a 50 Ohm microstrip line as input and the coplanar-to-microstrip transition as output, which are connected with gold wire bonds. All aspects are taking into account to obtain a more realistic result analyzing possible mismatching and losses due to these connections. The comparison is done in terms of S-parameters.

The four configurations are different in the following characteristics:

- Top left image (Config.1): the connection has made with a single wire bond between both parts.

- Top right image (Config. 2): home-made via-holes have been used in this case in the microstrip part with one wire bond for the central conductor line and one wire bond for each ground. The objective of this option is to have a more realistic coplanar junction between two parts.

- Bottom left image (Config. 3): use another coplanar-to-microstrip transition in the middle in order to join both parts, placing microstrip parts in the same side and coplanar parts joined with bonding wires (central conductor line and two grounds) too.

- Bottom right image (Config. 4): the connection is made with a single wire bond and furthermore including a wider section line following the 50 Ohm microstrip line to compensate the wire bond inductive effect.
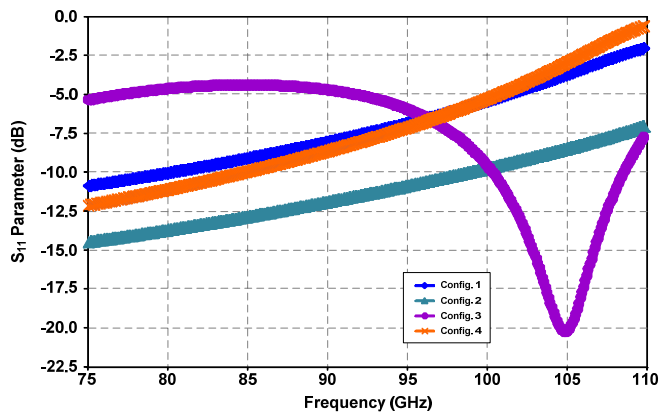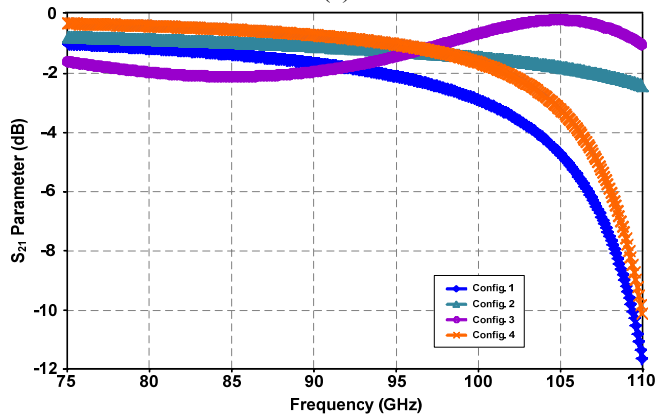
Fig.92. Electromagnetic Simulation Results of 4 Configurations (a) S_{11} Parameter, (b) S_{21} Parameter

From the results obtained shown in Fig.92, Configuration 2 (including home-made via-holes in microstrip part) would be the best option especially considering the losses in comparison with others configurations, obtaining an acceptable matching in the entire band too.

Fig.93. Different Options for the Monolithic´s Connections

The fabricated prototypes can be seen in Fig.93. Configuration 3 has not been fabricated due to its complexity for using another coplanar-to-microstrip transition. Two additional transitions have been necessary in input/output to place the air coplanar probes.
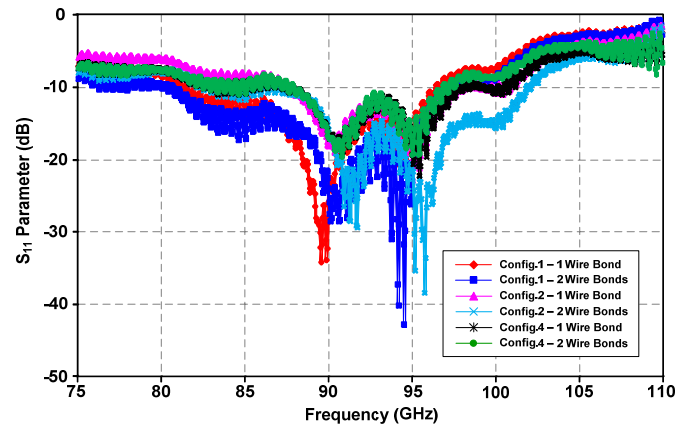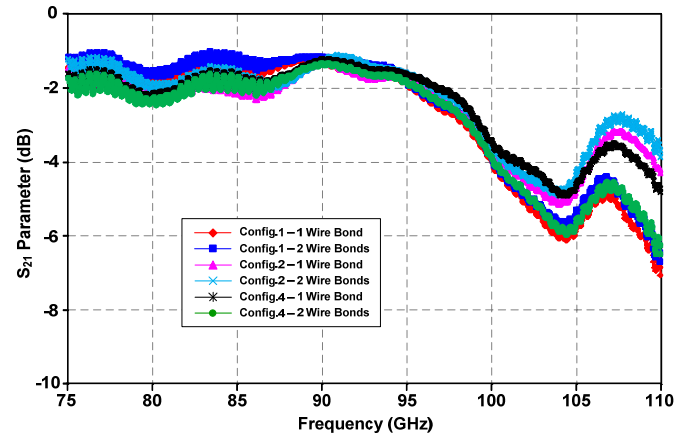
Fig.94. Measurements Results of 3 Configurations with One or Two Wire Bonds between External Coplanar-to-Microstrip Transitions and Input/Output of the Circuits (a) S_{11} Parameter, (b) S_{21} Parameter

From the comparison between the results obtained from the on wafer measurements (shown in Fig.94) of the 3 configurations and one or two wire bonds in external connections for each configuration, it can be concluded that Configuration 2 (with home-made via-holes to hold as much as possible the coplanar filed structure) with one or two wire bonds is the best solution to match the system.

F. WR-10 Waveguide Assembling of MMICs in W-band

This task has been developed by UNICAN. The general purpose transition previously presented was adapted to be used in a case housing a single LNA and in another case housing an LNA plus a detector to constitute a total power radiometer.
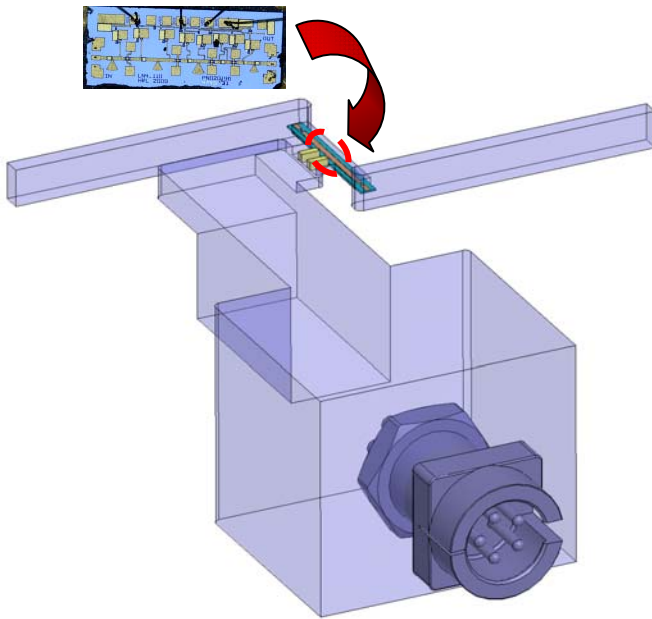
Fig.95. Redesign of the Back-to-Back Transition to measure LN4-110 in a Case Housing

For the design of the housing case, we start from the design of the back-to-back transition previously shown in subsection VI.A1.Previous simulation has been presented in [39]. This transition has been modified adding in the middle of the cut-off cavity an aperture to include the DC bias elements (resistances and capacitors) for the transistors which form the LNA MMIC. The cavity has been split into three narrow channels (suitable width for assembly of DC components) to avoid possible resonances in the cut-off cavity and its size has been increased in steps to host the DC connector as it can be seen in Fig.95. This structure will be valid for both: 4-stage LNA (LN4-110) and 5-stage (LN5-100).
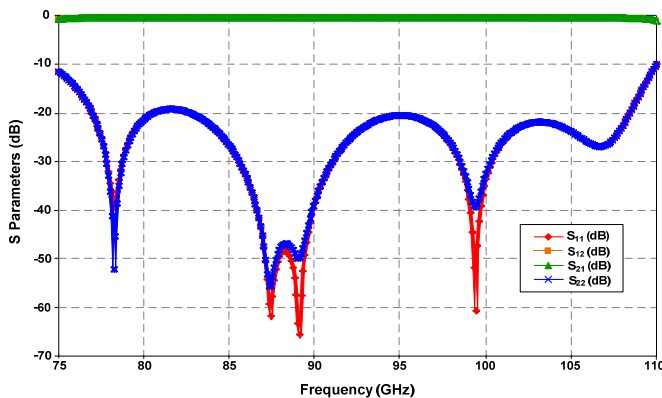
Fig.96. S-Parameters of the Transition Simulation

The results obtained in the simulation are presented in Fig.96, where we can see similar results of the back-to-back transition and a good matching in the entire band.
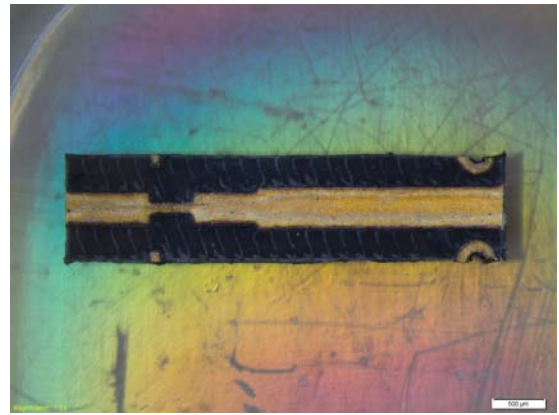
Fig.97. A Single Transition with Home-Made Vias for Assembly of the LN4-110 into the Metal Case

For fabrication, on one hand, the microstrip line sections which form each of the transitions have been fabricated with the previous configuration chosen: the home-made via-holes to be connected with the input/output of the LNA, maintaining the coplanar field structure and providing the minimum mismatching in this part of the assembly. Taking into account that LN4-110 and LN5-100 have a different MMIC length, and the mechanical structure will be the same for both cases, two different samples have been fabricated for both amplifiers. LN5-100 amplifier is longer than LN4-110 amplifier, therefore theirs transition lines have smaller length than the other ones. This difference is incremented in 50Ω-section, maintaining equal dimensions both transition sections and vias in two types. In Fig.97,it is shown a single transition for the assembly of the LN4-110 amplifier.
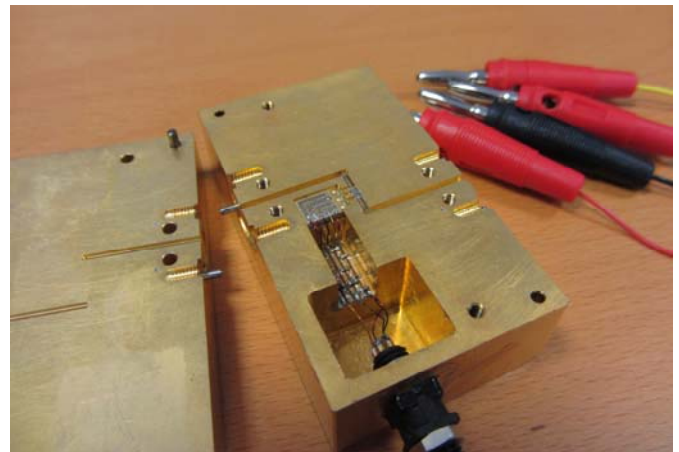
Fig.98. Complete WR-10 Waveguide Assembly for LN4-110 ($7 \times 4 \times 3$ cm^3)

On the other hand, the transition was fabricated by the same manufacturer that the back-to-back transition. The metal case is formed by two pieces split with the same technical concept.
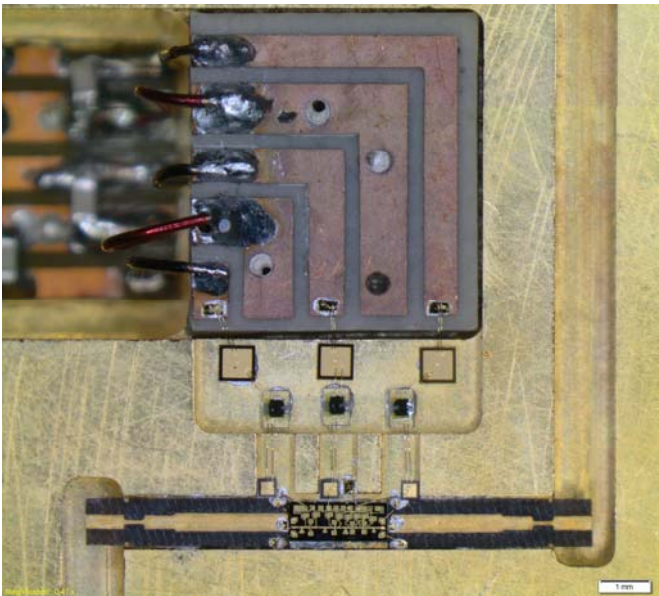
Fig.99. View in Detail of WR-10 Waveguide Assembly of LN4-110

Finally, the following step is to assemble the complete circuit with the LNA (LN4-110 or LN5-100), the single transitions with the home-made via-holes, the DC components (resistances and capacitors), substrates where the components will be placed, the DC bias connector, cables and the bonding gold wires necessary to join each component. Three prototypes have been fabricated, two for LN4-110 amplifiers and one for LN5-100 amplifier. The complete WR-10 waveguide assembly for a LN4-110 can be seen in Fig.98, and an internal detail where it can be seen the most important part of the assembly is shown in Fig.100.
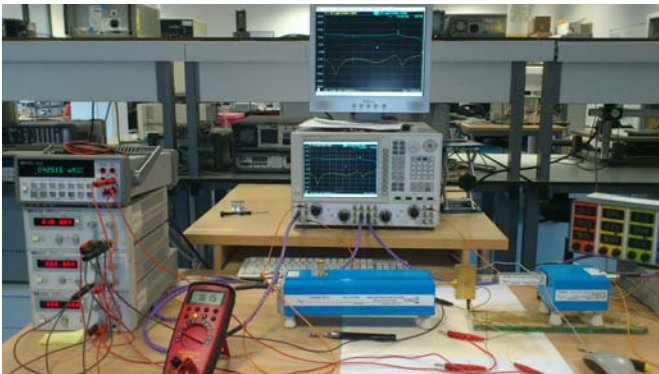
Fig.100. Setup for Waveguide Assembly S-Parameter Measurements in W-band (LN5-100 connected and biased)

Once three prototypes were mounted, S-parameter measurements were done. The setup in this case, for WR-10 waveguide assembly of LNAs is shown in Fig.100, realizing a waveguide calibration in this case and without the need of WR-10 waveguide-to-coplanar transitions, 1mm-coaxial cable, coplanar probes and the coplanar probes station.
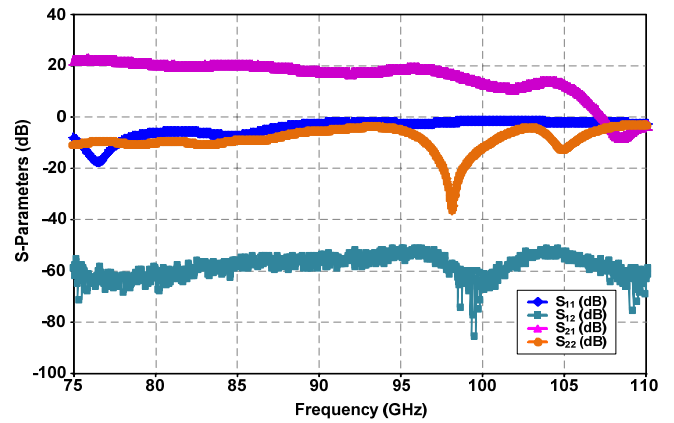
Fig.101. S-Parameters measured of the firstLN4-110 Amplifier

On one hand, the S-parameters obtained in the experimental measurements of the LN4-110 amplifiers are shown in Fig.101 (the first LN4-110 measured) and Fig.102 (the second one measured), where we can see a response similar to on wafer measurement results, showing a less gain in the final frequency range, it could be due to a displacement produced by the waveguide-to-microstrip transitions.
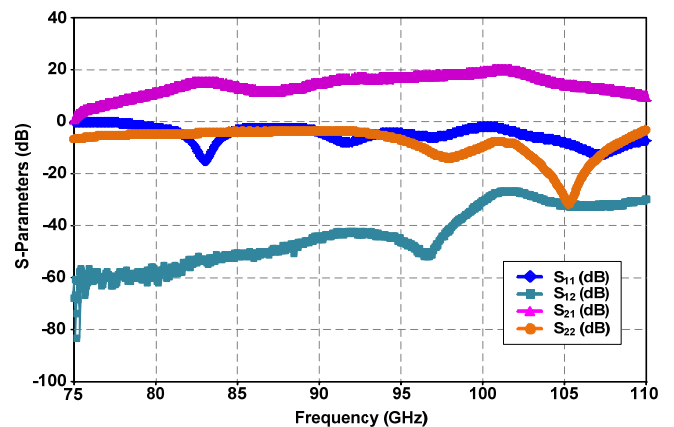
Fig.102. S-Parameters measured of the secondLN4-110 Amplifier

On the other hand, the LN5-100 measurements (see Fig.103) show an enhancement respect to the on wafer measurements and a similar gain to the datasheet. This LNA works from 70GHz up to 100GHz, but in the final 5GHz of the measured frequency range (100-105GHz), the gain does not decrease much (it could be due to the waveguide-to-microstrip transition too), making acceptable its response.
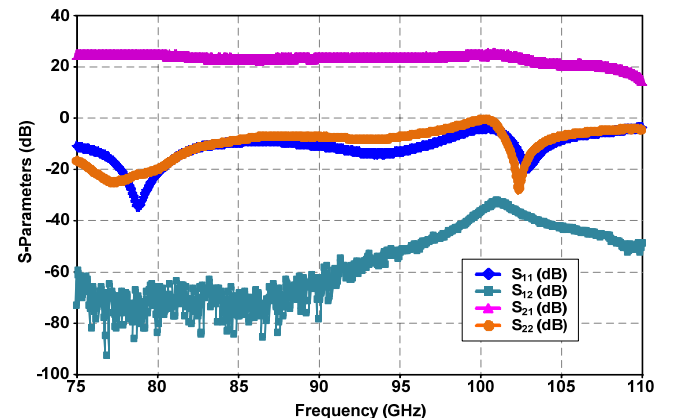
Fig.103. S-Parameters measured of the LN5-100 Amplifier

Along with a new LN5-100amplifier, a V1A detector was connected in its output pads using gold bonding wires (see Fig.104 and Fig.105). Moreover, taking into account that its output voltage will be DC voltage, the output transition was removed and substituted by a track with a central conductor and coplanar grounds to continue the same way of the output pads of the detector. Finally, this track was soldered with a final cable where a multimeter can be connected.
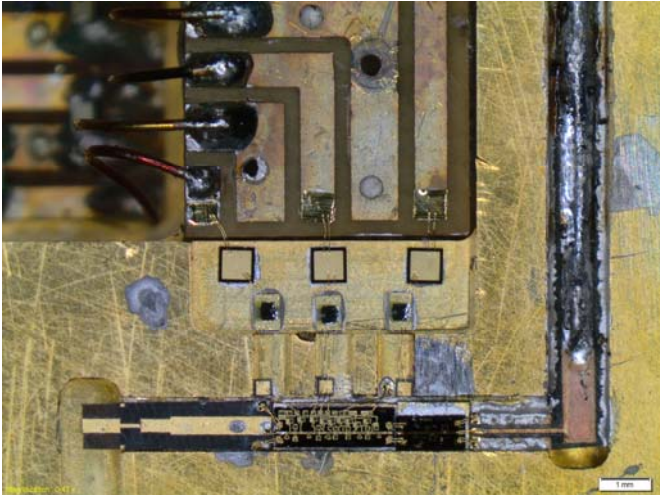
Fig.104. Assembly of LN4-110 + V1A into the Metal Case

Actually, there are not experimental measurements of this assembling due to problems with the mounted MMICs. A good input matching is obtained in the measurements, but no DC voltage was detected in the output of the system. Doubts about the junction of both MMICs or the proper operation existed.
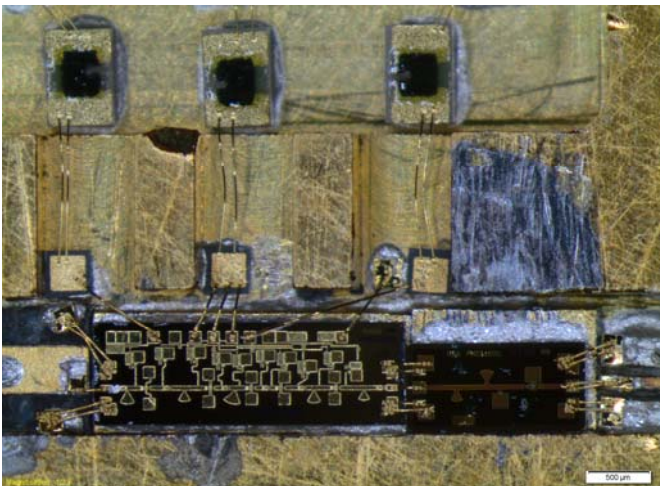
Fig.105. Detail of LN4-110 and V1A united with the Gold Bonding Wire

In order to check a good operation for both MMICs, measurements with the coplanar probes into the waveguide assembly were made. For these special measurements, the elimination of the common bonding wires and bonding wires of the input LNA was necessary, to separate two MMICs and place the probes on the input and output pads.
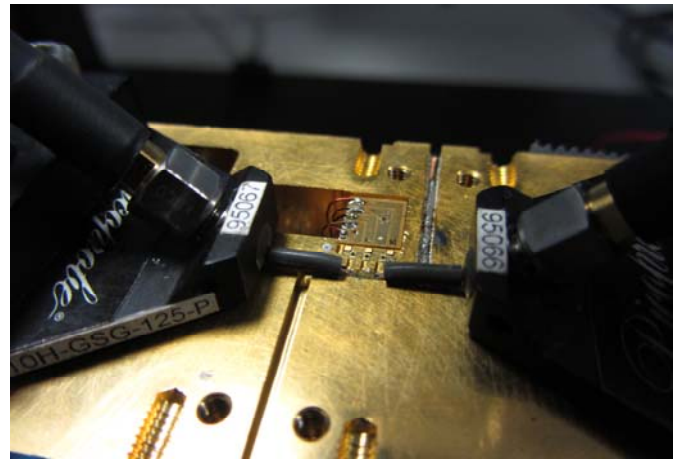
Fig.106. Testing of the LN5-100 in the Waveguide Assembly with the Coplanar Probes

From these measurements, we could prove the proper behavior of the LNA biased with the similar DC bias value for its drains and gates that LN5-100 on wafer measurements.

Regarding to the testing for V1A detector (see Fig.107), performing a frequency sweep and even increasing the input power to a high level (-15dBm approx.), the DC output voltage is practically null (0.987mV) when this voltage could reach 20-100mV, therefore, the V1A detector is damaged and it has to be substituted by other one. This problem found in the last measurements can be possibly due to ESD damage or overheating during the assembly. In future works, we will mount replacement detector in the metal case available from the MMIC´s provider.
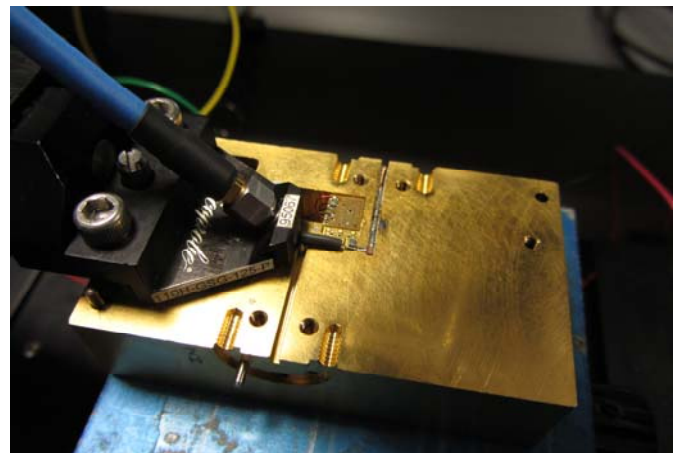
Fig.107. Testing of the V1A in the Waveguide Assembly with the Coplanar Probes

In the same way that waveguide assembly measurements, it could be interesting characterize the medium power amplifier (LSPA2), whose on wafer measurements are shown in section V, to be able to be integrated in the receiver system. The LSPA2 amplifier has not been mounted in the waveguide assembly because there are problems in the 3D electromagnetic simulation of the mechanical structure with undesired resonances due to the double aperture necessary to include DC bias elements of the lateral MMIC pads.

G. W-band Noise Figure Measurements Bench

A critical and important parameter in Low Noise Amplifiers is the Noise Figure, since it is the first element in a receiver chain and it needs to not introduce an excessive noise in the receiver. Therefore, it is desirable to measure this parameter. This task has been developed by UNICAN.

In our case, the two available commercial LNAs (LN4-110 and LN5-100 by HRL) present a 3dB Noise Figure, value obtained from datasheet.

A noise figure analyzer to measure the noise figure directly in W band frequencies is not available in the department laboratory, but an alternative setup is used in the noise measurements to solve the disadvantage.

The setup can be seen in Fig.108. This setup is fundamentally composed by: the OML receiver external module (converter in the system) which converter the W-band noise received to lower frequency noise; the swept signal generator needed for the mix of the external module, the noise figure analyzer and a noise source in W-band.

It is interesting to note that at least an LNA as part of the instrument is necessary in the setup to hold a good level for the noise figure analyzer, to obtain more gain and less noise in the measurements and it is included into the calibration system. Moreover, an isolator is placed between the instrument LNA and the converter.
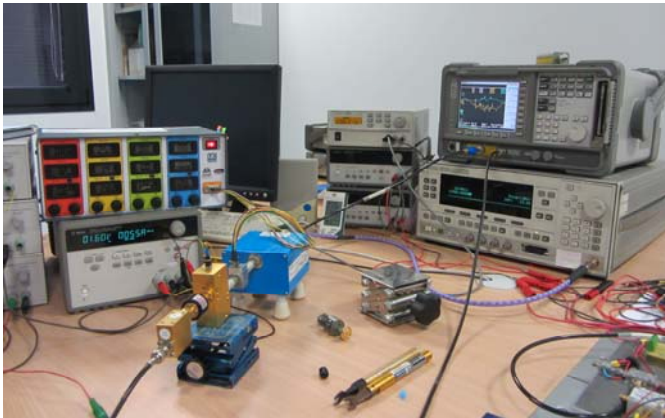
Fig.108. Noise Measurement Setup for available LNAs

The measurements have been done for both available LNAs in WR-10 waveguide assembly shown before (the second LN4-110 and the LN5-100), with a third LNA available in the department (fabricated by OMMIC) as the instrumentation LNA.

In Fig.109, the noise figure obtained for the LN4-110 amplifier is depicted. The typical noise figure given by the datasheet is 3dB, and the minimum noise figure obtained in our case is 5dB, having an average value of around 7.5dB.
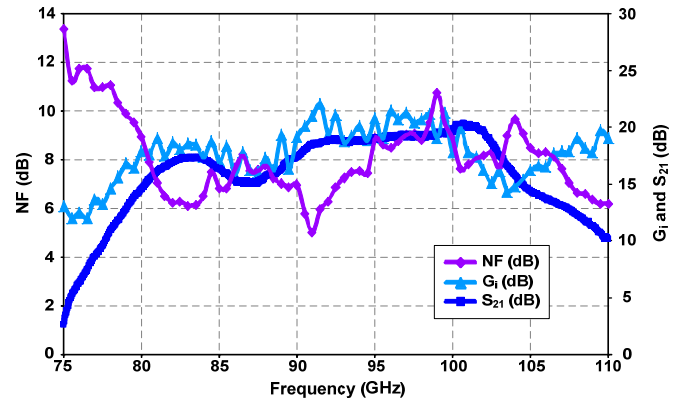
Fig.109. Figure Noise obtained for LN4-110 Amplifier

The noise figure of the LN5-100 can be seen in Fig.110.In this case, the noise figure obtained is better than LN4-110 noise figure, having a minimum level around 3 dB and an average value of around 5dB. In this LNA, the noise figure at higher frequencies is increased due to the operation frequency limit is 100GHz. Also, in both cases, the noise figure is more elevated in the first frequencies of the range.
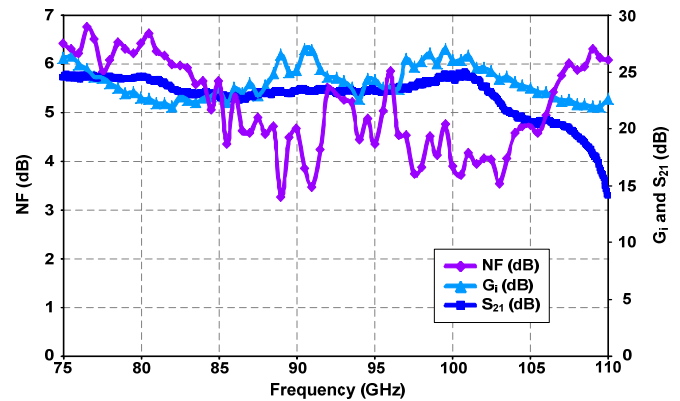
Fig.110. Figure Noise obtained for LN5-100 Amplifier

These measurement results are provisional until the receiver could be improved being the noise source attenuated to provide an Excess Noise Ratio (ENR) in the same order that the noise figure under test.

H. Hybrid Detector based on Discrete Zero Bias Diodes (ZBD VDI)

Given the sensibility of the commercial detectors shown in subsections before during its handling and measurements, we decided to develop an alternative detector with an own design. In this way, we could fabricate several units in the department with low cost and we can control the design modifying the different parts of the same one if we obtained an undesired response in the measurements such as a frequency shift, a bad input matching or even a low output voltage. This task has been developed by UNICAN.
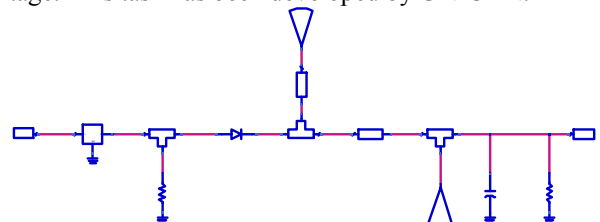
Fig.111. Simplified Schematic Diagram of the Detector Design

The first design of the own detector is shown in Fig.111. This design is composed fundamentally by: the complete large-signal equivalent circuit model of a Schottky zero bias diode (modeling shown in subsection III.C), a coplanar-to-microstrip transition in the input with the gold bonding wire to connect it to the circuit substrate, a matching network between the transition and the diode (composed by microstrip lines and a 51Ω-SMD resistance model), a virtual short using radial stubs, a RC filter and the pad with the cable for output voltage. The final design fabricated is shown in Fig.112.
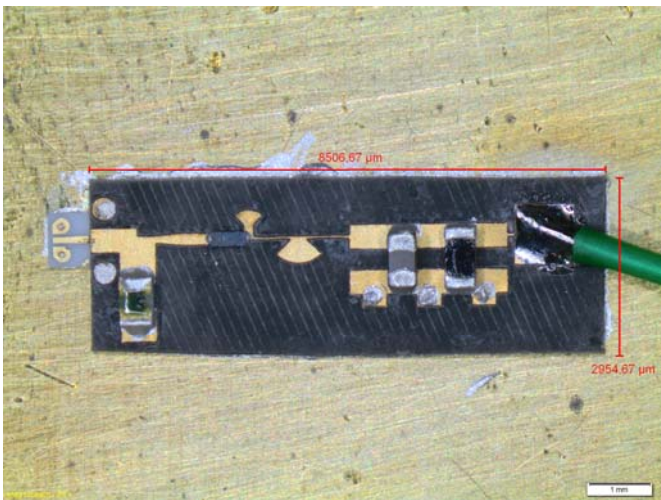
Fig.112. Schematic of the Detector Design

The input matching obtained in the experimental measurements is compared with simulation results (see Fig.113). An important frequency shift in the input matching is found. We are analyzing in depth the detector design to know which elements are responsible for this behavior.
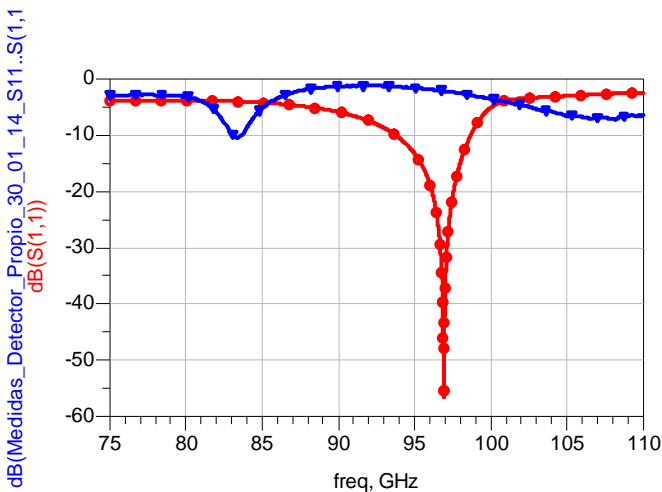
Fig.113. Comparison between Simulation and Measurement Input Matching

The DC voltage detected in the output detector is depicted in Fig.114. It can be seen a greater value detected in around 83GHz is obtained, in the same frequency where obviously the input matching is better.
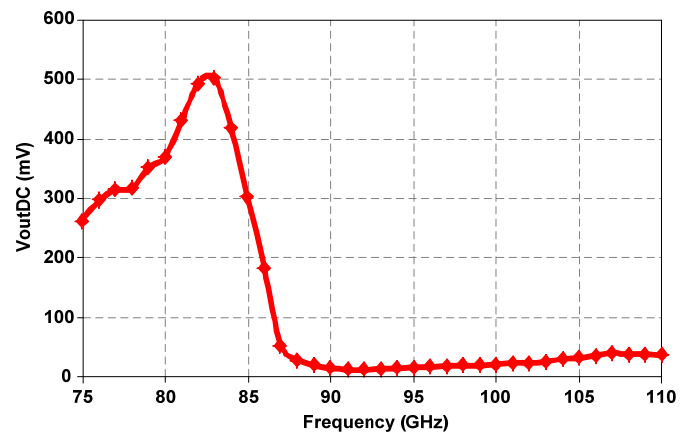
Fig.114. DC Voltage Detected in the Output Detector

Output voltage versus input power is plotted in Fig.115.
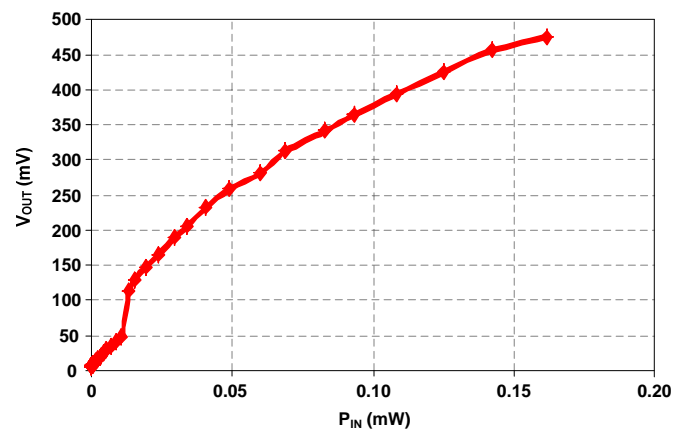
Fig.115. Pin-Vout Curve of the Detector Measurements (at 83.4GHz)

Regarding to the input matching and the output DC voltage, the detector has moved its response from 97GHz down to 83.4GHz. Analyzing the design, an element which can produce this displacement is the 51Ω-SMD resistance model used. This resistance model was optimized previously up to 30GHz and its response could be quite different extrapolating this model up to 110GHz. Furthermore, a new equivalent circuit model more accurate has been obtained for this 51Ω resistance and for a 100Ω resistance.

Fig.116. Arrangement for on Wafer Characterization of SMD Resistances

In this way, new assemblies with these resistances could be eventually mounted (see Fig.116) with the same configuration that the detector design (only one access with the coplanar-to-microstrip transition and the other pad connected to a via hole ground) and with a coplanar-to-microstrip transition in each pad.

Fig.117. Equivalent Circuit Model of SMD Resistance (51Ω)

An adjustment between experimental measurements and simulation circuit has been realized optimizing the elements and the final equivalent circuit models of these resistances can be seen in Fig.117 for the case of 51Ω-SMD resistance and in Fig.118 for the 100Ω-SMD resistance.

Fig.118. Equivalent Circuit Model of SMD Resistance (100Ω)

The detector design was re-simulated taking into account this new model and adding some new parasitic elements in the equivalent circuit model of the zero bias diode too, because in this design the ZBD was mounted on flip-chip and some parasitic elements affect the performance therefore they have to be taken into account in this frequencies.

Fig.119. Comparison between Corrected Simulation and Measurement Input Matching

The simulation corrected with these aspects before mentioned is compared with measurements in Fig.119. Now we can see better agreement between simulation and measured results with a more similar form in both cases. Now we are improving the detector design including these aspects to correct its response to be matched at the desired frequency of 97GHz.

Moreover, we are interested in adapt this design to be included in the WR-10 waveguide assembly for the complete radiometer structure.

VII. MMW IMAGES IN BIOMETRIC APPLICATIONS

This section describes the application of MMW images in the field of biometric recognition. This task has been developed by UAM. Biometric recognition is the science which studies the recognition of humans through one or several physiological and/or behavioural characteristics [50]. Many biometric characteristics are used to identify individuals: fingerprint, signature, iris, voice, face, hand, etc. Biometric traits such as the face, hand, gait and ear are usually acquired with cameras working at visible frequencies of the electromagnetic spectrum. Such images are affected by, among other factors, lighting conditions and the body occlusion (e.g., clothing, make up, hair, etc.). In order to circumvent these limitations, researchers have proposed the use of images acquired at others spectral ranges: X-ray, infrared, millimeter (MMW) and submillimeter (SMW) waves [51]. The images captured beyond the visible spectrum overcome, to some extent, some of the mentioned limitations; furthermore, they are more robust to spoofing than other biometric images/traits. Among the spectral bands out of the visible spectrum, the millimeter waves (with frequency in the band of 30-300 GHz) present interesting properties that can be exploited in biometrics (see Fig. 120): ability to pass through cloth and other occlusions, innocuous to health, low intrusiveness, and the recent deployment and rapid progress of GHz-THz systems in screening applications.

In spite of the previous advantages, to date, there are just a few works on this field of research. Specifically, just one working with real data [52], and some others based on BIOGIGA database, which is a synthetic database [53]-[56]. In [52], Alefs et al. proposed a holistic recognition approach based on the texture information of the MMW images. On the other hand, the works by Moreno-Moreno et al. [53]-[55] proposed a biometric system based on geometric measures between different silhouette landmarks of the contour. There is also a previous work [56] in which some baseline techniques such as the contour coordinates, used as the shape descriptors, and Euclidean distance and dynamic time warping algorithm, used as similarity measures, are used in order to build a biometric system based on the contour information. This shortage of biometric recognition research based on MMW images is mainly due to the lack of databases of images of people acquired at 94 GHz. This lack is a consequence of: i) the privacy concerns these images present, and ii) most of the imaging systems working at the MMW/SMW band are either in prototype form or not easily accessible for research.

Fig. 120. Examples of MMW Body Images for Active/Passive Systems in Outdoors and Indoors Scenarios, taken from [51]. From left to right: Outdoors Passive MMW Image, Indoors Passive MMW Image, Active MMW Image

This section extends the previous work [56] by comparing several shape descriptors of the body contours (contour coordinates, shape contexts, Fourier descriptors and silhouette landmarks) and two similarity measures (Euclidean distance and a dynamic programming method) with the objective of finding the best configuration in terms of biometric recognition performance. This is inspired by previous works, which show that recognition through the shape and boundary of traits such as the hand or the signature are fairly reliable. Fig. 121 draws a simple diagram explaining the different stages of the considered body shape biometric system. As can be seen, there are three principal stages: the contour extraction, the parameterization stage and the comparison stage.
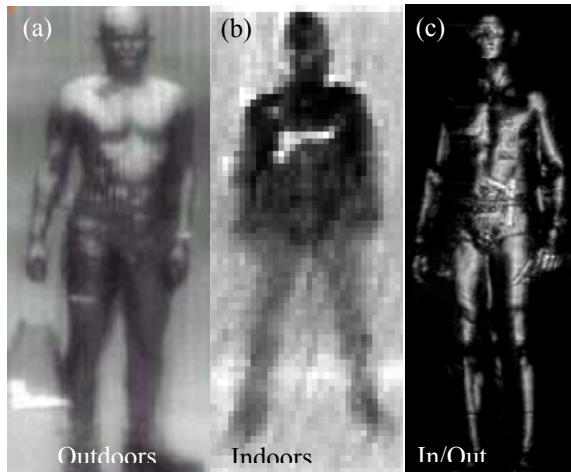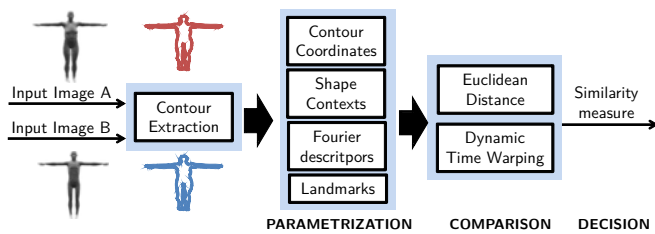

Fig. 121. General Scheme of the MMW Body Shape-based Biometric System. First the Silhouette Contour is extracted from the Input MMW Images, then four Types of Parameterization Techniques are applied with two Comparison Methods, and finally Results are obtained for all Different Configurations

The experimental work is carried out using a database of synthetic MMW images, BIOGIGA [54], collected from 50 people (25 males and 25 females). This database contains images simulating passive and active systems in indoors and outdoors scenarios. Only the data corresponding to a passive system in outdoors scenarios was considered for the experiments presented in this work.

Four shape descriptors were extracted from the body contours: 1) Contour coordinates (CC), which are the 2-dimensional vector which specifies the x and y position of every single point within the silhouette of the body and are used as the baseline feature approach. 2) Shape contexts (SC), which describe a specific point as a histogram containing information about the position of all points of the shape with respect to this specific one [57]. 3) Fourier descriptors (FD) [58], which are computed as the Fourier

transform of the contour coordinates transformed as a sequence of complex numbers. These descriptors are simple to compute and robust against translations and rotations. 4) Silhouette landmarks (LM), which consist of 14 points which represent the most singular parts of the people silhouette, among them: head, neck, hands, underarms, waist, hip, pubis and feet. This is a reduced set of the key points obtained in our previous work [53].

Regarding the classification stage, two types of distances are employed: 1) Euclidean distance (ED), which has the restriction that distances need to be computed between sequences of the same length, and 2) dynamic time warping (DTW), a more complex technique, which can obtain a cumulative distance between two strings of coordinates which do not necessarily have to share the same dimension.

Fig. 122 shows the experimental results obtained in terms of equal error rate (EER) for the eight possible configurations of feature descriptors and similarity measures. Also, three experimental protocols were used: 1:1, 2:1 and 3:1, the first number indicating the number of images used for model training and the second number indicating the number of images used for testing. First, we can observe that the EER of the system decreases as the number of training images increases (Protocol 3:1). Regarding the average performance between all protocols, the best approaches are in order: SC-DTW (3.96%), LM-ED (4.91%), FD-ED (5.41%) and CC-DTW (6%). For the 3:1 protocol, the best EER of 1.33% was achieved for the CC-DTW approach. However, considering the other two protocols, it can be seen that the performance of the CC-DTW approach is worse compared to other cases. For example, the SC-DTW produces lower EER rates for protocols 1:1 and 2:1 although it requires a much higher computational time. In the case of the FD-ED approach, we observe that the number of training images do not imply considerable variations in the performance. This supports the fact that FD are more robust against rotations since each one of the three possible training images has different cameras angles. Regarding the LM-ED approach, we see that using a vector with a dimensionality quite smaller than the vectors used in any of the previous approaches, can produce comparable results to the best approaches. However, in a real database we believe the localization of these landmarks points would be not as robust as in this synthetic database.
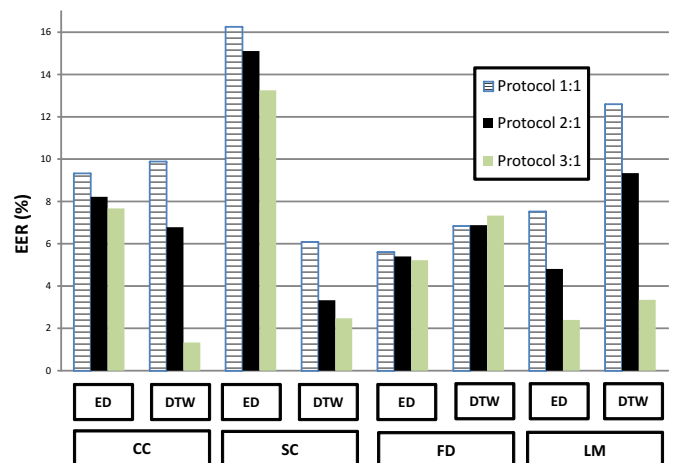

Fig. 122. Results in terms of EER of the Biometric System using MMW Body Images for the eight Approaches Protocols 1:1, 2:1 and 3:1. ED=Euclidean Distance. DTW=Dynamic Time Warping, CC=Contour Coordinates, SC=Shape Contexts, FD=Fourier Descriptors and LM=Landmarks

VIII. Conclusions

The CSD2008-00068 TERASENSE CONSOLIDER project permitted the extension upwards in frequency of the previous background of the microwaves research group partners. This article compiles some of the technology developments in the frame of the TERASENSE work package "THz Device Technology Laboratory", particularly in aspects like antenna manufacturing, characterization of active and passive devices, design and assembling of circuits and data processing. An initial great jump has been done, which, if the activities in these THz bands continue in the future, may allow settling a solid background for development of new applications.

Acknowledgement

References

[1] A. García-Pino, J. Gutiérrez, J. Montero-de-Paz, [et al]. "TERASENSE: THz Device Technology Laboratory". XXVIII Simposium Nacional de la Unión Científica Internacional de Radio (URSI 2013). Septiembre 2013. Santiago de Compostela

[2] Siegel, P.H. Terahertz Technology. IEEE Transactions on Microwave Theory And Techniques, Vol. 50, No. 3. March 2002

[3] Räisanen, A.V. Challenges of Terahertz. The Second European Conference on Antennas and Propagation, EuCAP 2007. 2007

[4] Oka, S.; Togo, H.; Kukutsu, N.; Nagatsuma, T. "Latest Trends in Millimeter-Wave Imaging Technology". Progress In Electromagnetics Research Letters, Vol. 1, 197–204, 2008

[5] Shur, M. Terahertz technology: devices and applications. Proceedings of ESSCIRC, Grenoble, France. 2005

[6] S. Yeom, D.-S. Lee, H. Lee, J.-Y. Son, V.P. Guschin, "Distance Estimation of Concealed Objects with Stereoscopic Passive Millimeter-Wave Imaging", Progress in Electromagnetics Research Letters, Vol. 115, 399-407, 2011

[7] P.H. Siegel and R.J. Dengler, "Terahertz Heterodyne Imaging: Introduction and Techniques," Int. Journal of Infrared and Millimeter Waves, v.27, no. 4, April 2006

[8] Essen, H.; Fuchs, H.; Hägelen, M. [et al.]. Concealed Weapon Detection with Active and Passive Millimeterwave Sensors, Two Approaches. http://duepublico.uni-duisburg-essen.de/servlets/ DerivateServlet/Derivate-14694/Final_Papers/GM0004-F.pdf

[9] Stanko, S.; Nötel, D.; WAHLEN, A.; [et al.]. 2008. Active and Passive mm-Wave imaging for Concealed Weapon Detection and Surveillance. 33rd International Conference on Infrared, Millimeter and Terahertz Waves, IRMMW-THz 2008

[10] Tessmann, A.; Kudszus, S.; Feltgen, T.; [et al] 2002. Compact single-chip Wband FMCW radar modules for commercial high resolutions sensor applications. IEEE Transactions on Microwave Theory and Techniques, Vol. 50, Issue 12

[11] Sato, M.; Sato, H.; Hirose, T.; [et al] 2007. Compact receiver module for a 94GHz band passive millimetre-wave imager. In Special Issue on Asia Pacific Microwave Conference 2007

[12] N. Amar, J. Gutiérrez, A. Tazón, F. Cátedra, A. Mediavilla. "Array Lineal de Antenas planas Excitadas por Ranuras en la Banda W". XXVII Simposium Nacional de la Unión Científica Internacional de Radio (URSI 2012). 12-14 Septiembre. Elche. (.ISBN 9788469543269)

[13] O. Fernández, A. Gómez, J. Gutiérrez, A. Tazón, A. Vegas. "Enhancement of the radiation properties of a lineal array of planar antennas with a chiral metamaterial cover". Proceedings of the 2013 Spanish Conference on Electron Devices (CDE), pp. 223 - 226, 2013

[14] J. Gutiérrez, O. Fernández, J.P. Pascual, A. Gómez, A. Tazón, A. Vegas, N. Amar. "Design and Fabrication of a W-Band Linear Array of Planar Antennas and Study for the Enhancement of its Radiation Properties with a Chiral Metamaterial Cover". 4th International Conference on Multimedia Computing and Systems. 14-16 Abril 2014. Marrakesh. Marruecos

[15] O. Fernández, A. Gómez, J. Gutiérrez, A. Tazón, A. Vegas. "Array Lineal de Parches Excitados por Ranura con Radiación Mejorada Mediante Cobertura Quiral". XXVIII Simposium Nacional de la Unión

Científica Internacional de Radio (URSI 2013). Septiembre 2013. Santiago de Compostela

[16] Nova, E.; Rodrigo, D.; Romeu, J. &Jofre, L., "94 GHz cassegrain reflector antenna performance characterization", Antennas and Propagation (EUCAP), 2012 6th European Conference on, 2012, 3442 - 3445

[17] A.G.Pino, N.LLombart, B.Gonzalez-Valdes and O. Rubiños; "A Bifocal Ellipsoidal Gregorian Reflector System for THz Imaging Applications," IEEE Transactions on Antennas and Propagation, vol. 60, no. 9, pp. 4119–4129, Sep. 2012

[18] J. Montero-de-Paz, I. Oprea, V. Rymanov, S. Babiel, E. García-Muñoz, A. Lisauskas, M. Hoefle, Á. Jimenez, O. Cojocari, D. Segovia-Vargas, M. Palandöken, T. Tekin, A. Stöhr, and G. Carpintero, "Compact Modules for Wireless Communication Systems in the E-Band (71–76 GHz)", Journal of Infrared, Millimeter, and Terahertz Waves, vol. 34, Issue 3-4, pp 251-266, April 2013

[19] J. Montero-de-Paz, E. Ugarte-Muñoz, L. E. García-Muñoz, I. Cámara Mayorga, D. Segovia-Vargas, "Meander Dipole Antenna to Increase CW THz Photomixing Emitted Power", IEEE Transactions on Antennas and Propagation, submitted 21st February 2014

[20] J. Montero-de-Paz, E. Ugarte-Muñoz, L.E. Garcia-Muñoz, D. Segovia-Vargas, D. Schoenherr, I. Oprea, A. Amrhein, O. Cojocari, H.L. Hartnagel, "Millimeter-wave receiver based on a folded dipole antenna and Schottky diode for maximum power transfer", (2012) Proceedings of 6th European Conference on Antennas and Propagation, EuCAP 2012, art. no. 6206286, pp. 1259-1262, 26-30 March, Prague, Czech Republic

[21] S. Preu, G.H. Döhler, S. Malzer, L.J. Wang, H. Lu, and A.C. Gossard, "Tunable, Continuous Wave Terahertz Photomixer Sources and Applications" (review article), Journal of Applied Physics 109, 061301-1-56, 2011

[22] Mariano Barba, Gerardo Perez-Palomino, José A. Encinar, Manuel Sierra Castañer, Alfonso Muñoz Acevedo, Raymond Dickie, Michael Bain, Paul Baine and Robert Cahill, "Caracterización de un reflectarray de cristal líquido en banda W (100 GHz)", Libro de Actas de URSI 2014, 3-5 de Septiembre, Valencia

[23] G. Perez-Palomino, R. Florencio, J.A. Encinar, R. Dickie, R. Cahill, P. Baine, M. Bain, M. Barba, R. Boix, "Accurate and Efficient Modeling to Calculate the Voltage Dependence of Liquid Crystal Based Reflectarray Cells", IEEE Transactions on Antennas and Propagation Aceptado, Disponible en Early-View

[24] Gerardo Perez-Palomino, Mariano Barba, José A. Encinar, Manuel Arrebola, Raymond Dickie, Michael Bain, Paul Baine, Robert Cahill, "Antena doble reflector de barrido electrónico en banda W (100 GHz) basada en un reflectarray de cristal líquido", Libro de Actas de URSI 2014, 3-5 de Septiembre, Valencia

[25] G. Perez-Palomino, M. Barba, M.Bain, J.A. Encinar, R. Cahill, R. Dickie, P. Baine, and M. Arrebola, "Dual Reflector Antenna with a Liquid Crystal-Based Sub-Reflectarray for Beam Scanning at 100 GHz" Sent to IEEE Trans. Antennas Propagation

[26] C. A. Leal-Sevillano, T. J. Reck, C. Jung-Kubiak, G. Chattopadhyay, J. A. Ruiz-Cruz, J. R. Montejo-Garai, J. M. Rebollar, "Silicon Micromachined Canonical E-Plane and H-Plane Bandpass Filters at the Terahertz Band", IEEE Microwave and Wireless Components Letters, vol. 23, no. 6, pp. 288-290, June 2013

[27] C. A. Leal-Sevillano, K. B. Cooper, J. A. Ruiz-Cruz, J. R. Montejo-Garai, J. M. Rebollar, "A 225 GHz Circular Polarization Waveguide Duplexer Based on a Septum Orthomode Transducer Polarizer", IEEE Transactions on Terahertz Science and Technology, vol. 3, no. 5, pp. 574-583, September 2013

[28] C. A. Leal-Sevillano, G. Pisano, J. R. Montejo-Garai, B. Maffei, J. A. Ruiz-Cruz, M. W. Ng, J. M. Rebollar, "Development of Low Loss Waveguide Filters for Radio-Astronomy Applications", Infrared Physics and Technology, vol. 61, pp. 224-229, 2013

[29] C. A. Leal-Sevillano, J. R. Montejo-Garai, J. A. Ruiz-Cruz, J. M. Rebollar, "Experimental Comparison of Waveguide Filters at W-Band Implemented by Different Machining Processes and Split-Block", Journal of Electromagnetic Waves and Applications, vol. 27, no. 18, pp. 2390-2394, 2013

[30] C. A. Leal-Sevillano, Y. Tian, M. J. Lancaster, J. A. Ruiz-Cruz, J. R. Montejo-Garai and J. M. Rebollar, "A Micromachined Dual-Band Orthomode Transducer", IEEE Transactions on Microwave Theory and Techniques, vol. 62, no. 1, pp. 55-63, January 2014

[31] K. Zeljami, J. Gutiérrez, J. P. Pascual, T. Fernández, A. Tazón, M. Boussouis. "Characterization and modeling of Schottky diodes up to 110GHz for use in both flip-Chip and wire-bonded assembled environments". Progress In Electromagnetics Research, Vol. 131, pp.457-475, 2012

[32] K. Zeljami. Caracterización y Modelado de Dispositivos Semiconductores Para Uso en Sistemas de Telecomunicaciones a Frecuencias de Terahercios. Tesis Doctoral. University of Cantabria. Available in: http://bucserver01.unican.es/xmlui/handle/10902/3089

[33] K. Zeljami, T. Fernández, J.P. Pascual, A. Tazón, M. Boussouis, "Modelado de Diodos Schottky para Aplicaciones a Frecuencias de Terahercios". XXV Symposium Nacional de la Unión Cientifica Internacional de Radio (URSI-2010). 14-16 Septiembre. Bilbao

[34] K. Zeljami, J. Gutiérrez, J.P. Pascual, T. Fernández, A. Tazón. "Caracterización de Transiciones Coplanar-Microstrip en Banda W". XXVI Symposium Nacional de la Unión Cientifica Internacional de Radio (URSI-2011). 07-09 Septiembre. Leganés (ISBN: 978-84-933934-5-8)

[35] K. Zeljami, J. Gutiérrez, J.P. Pascual, T. Fernández, A. Tazón, M. Boussouis. "Caracterización de Diodos Schottky para Banda W". XXVII Simposium Nacional de la Unión Científica Internacional de Radio (URSI 2012). 12-14 Septiembre. Elche. (.ISBN 9788469543269)

[36] M. Arias, L. De La Fuente, J.P. Pascual, A. Tazón. "Amplificador MhemtCascodo de Bajo Ruido a 100 GHz". XXIV Symposium Nacional de la Unión Cientifica Internacional de Radio (URSI-2009). 16-18 Septiembre. Santander (ISBN: 978-84-8102-550-7)

[37] M. Arias, L. De La Fuente, J.P. Pascual, A. Tazón. "Diseño de un Amplificador MHEMT de Media Potencia a 94-100 GHz". XXIV Symposium Nacional de la Unión Cientifica Internacional de Radio (URSI-2009). 16-18 Septiembre. Santander (ISBN: 978-84-8102-550-7)

[38] P. de Paco, A. Tazón, O. Menéndez, J.P. Pascual, J. Parrón, T. Fernández, G. Junkin, J. Gutiérrez, K. Zeljami. Ponencia: "Sub-Millimeter Wave Receivers". XXV Simposium Nacional de la Unión Científica Internacional de Radio (URSI 2010). Septiembre 2010. Bilbao

[39] J. Gutiérrez, K. Zeljami, T. Fernández, J.P. Pascual, A. Tazón. "Caracterización de Componentes y Balance de Potencia para Radiómetro en Banda W". XXVII Simposium Nacional de la Unión Científica Internacional de Radio (URSI 2012). 12-14 Septiembre. Elche. (.ISBN 9788469543269)

[40] J. Gutiérrez, K. Zeljami, J.P. Pascual, T. Fernández, A. Tazón, A. Mediavilla, E.S. Pana. "Yield-Oriented Design Protocol and Equivalent Circuit Model for W-Band E-Plane Waveguide-to-Microstrip Transitions". International Journal of RF and Microwave Computer-Aided Engineering. (2013) DOI: 10.1002/mmce.20716. Volume 24, Issue 1, pp. 77-91. Jan. 2014

[41] J. Gutiérrez, K. Zeljami, T. Fernández, J.P. Pascual, A. Tazón, Á. Mediavilla, S. Pana. "Transición Guía de Onda-Microstrip en Banda W". XXVI Symposium Nacional de la Unión Cientifica Internacional de Radio (URSI-2011). 07-09 Septiembre. Leganés (ISBN: 978-84-933934-5-8)

[42] M.R. Fetterman, J. Grata, G. Jubic, W.L. Kiser, Jr., A. Visnansky, "Simulation, acquisition and analysis of passive millimeter-wave images in remote sensing applications", Optics Express, vol. 16, nº. 25, pp. 20503–20515, Dec 2008

[43] E. L. Stein, Jr., C. A. Schuetz, R. D. Martin, J. P. Samluk, J. P. Wilson, D. G. Mackrides, J. A. Murakowski, M. Murakowski, D. W. Prather, "Passive Millimeter-Wave Cross Polarization Imaging and Phenomenology" Proc. of SPIE, vol. 7309, no. 730902, Apr. 2009. http://dx.doi.org/10.1117/12.819033

[44] D. Bourreau, A. Péden, S. Le Maguer, "A Quasi-Optical Free-Space Measurement Setup Without Time-Domain Gating for Material Characterization in the W-Band," IEEE Trans. on Instrumentation and Measurement, vol. 55, nº 6, pp. 2022-2028, Dec. 2006

[45] P. F. Goldsmith, Quasioptical Systems, IEEE Press, 1998

[46] www.janostech.com

[47] C. Granet, G.L. James, R. Bolton, G. Moorey, "A Smooth-Walled Spline-Profile Horn as an Alternative to the Corrugated Horn for Wide Band Millimeter-Wave Applications", IEEE Trans. on Antennas and Propagation, vol. 52, nº3, pp. 848-854, Mar. 2004

[48] www.feko.info

[49] J. Gutiérrez, J.P. Pascual, T. Fernández, P. De Paco, A. Tazón, J. Parrón, O. Menéndez. "Configuraciones Para Radiómetro De Potencia Total En Banda W". XXV Symposium Nacional de la Unión Cientifica Internacional de Radio (URSI-2010). 14-16 Septiembre. Bilbao

[50] A. Jain, A. Ross, and S. Prabhakar, "An Introduction to Biometric Recognition", IEEE Trans. on CSVT. Vol. 14, No. 1, pp. 4-20, 2004

[51] M. Moreno-Moreno, J. Fierrez, and J. Ortega-Garcia, "Biometrics Beyond the Visible Spectrum: Imaging Technologies and Applications", in Proceedings of BioID-Multicomm 2009, LNCS 5707, 154–161, Springer (September 2009)

[52] B.G. Alefs, R.J.M. den Hollander, F.A. Nennie, E.H. van der Houwen, M. Bruijn, W. van der Mark, and J.C. Noordam, "Thorax biometrics from Millimetre-Wave images", Pattern Recognition Letters 31(15), 2357–2363 (2010)

[53] M. Moreno-Moreno, J. Fierrez, R. Vera-Rodriguez and J. Parron, "Simulation of Millimeter Wave Body Images and its Application to Biometric Recognition", in Proc. International Conferencie SPIE, Defense Security and Sensing, SPIE, 2012

[54] M. Moreno-Moreno, J. Fierrez, P. Tome, R. Vera-Rodriguez, J. Parron and J. Ortega-Garcia, "BioGiga: Base de datos de imágenes sintéticas de personas a 94 GHz con fines biométricos", in Proc. of XXVI Simposium Nacional de Union Cientifica Internacional de Radio, URSI 2011, Madrid, Spain, September 2011

[55] M. Moreno-Moreno, J. Fierrez, R. Vera-Rodriguez and J. Parron "Distance-based feature extraction for biometric recognition of millimeter wave body images", in Proc. IEEE Intl. Carnahan Conf. on Security Technology, ICCST, 2011, pp. 1–6

[56] E. Gonzalez-Sosa, R. Vera-Rodriguez, J. Fierrez, and J. Ortega-Garcia, "Body shape-based biometric recognition using millimeter wave images", in Proc. IEEE Intl. Carnahan Conf. on Security Technology, ICCST, 2013

[57] S. Belongie, J. Malik, and J. Puzicha, "Shape matching and object recognition using shape contexts", IEEE Transactions on Pattern Analysis and Machine Intelligence, vol. 24, no. 4, pp. 509–522, 2002

[58] E. Persoon and K.-S. Fu, "Shape discrimination using fourier descriptors", IEEE Transactions on Systems, Man and Cybernetics, vol. 7, no. 3, pp. 170–179, 1977